

ANALYSIS OF REGENERATIVE COOLING IN LIQUID PROPELLANT
ROCKET ENGINES

A THESIS SUBMITTED TO
THE GRADUATE SCHOOL OF NATURAL AND APPLIED SCIENCES
OF
MIDDLE EAST TECHNICAL UNIVERSITY

BY

MUSTAFA EMRE BOYSAN

IN PARTIAL FULFILLMENT OF THE REQUIREMENTS
FOR
THE DEGREE OF MASTER OF SCIENCE
IN
MECHANICAL ENGINEERING

DECEMBER 2008

Approval of the thesis:

**ANALYSIS OF REGENERATIVE COOLING IN LIQUID PROPELLANT
ROCKET ENGINES**

submitted by **MUSTAFA EMRE BOYSAN**, in partial fulfillment of the requirements for the degree of **Master of Science in Mechanical Engineering Department, Middle East Technical University** by,

Prof. Dr. Canan ÖZGEN
Dean, Graduate School of Natural and Applied Sciences

Prof. Dr. Süha ORAL
Head of Department, Mechanical Engineering

Assoc. Prof. Dr. Abdullah ULAŞ
Supervisor, Mechanical Engineering Dept., METU

Examining Committee Members:

Prof. Dr. Haluk AKSEL
Mechanical Engineering Dept., METU

Assoc. Prof. Dr. Abdullah ULAŞ
Mechanical Engineering Dept., METU

Prof. Dr. Hüseyin VURAL
Mechanical Engineering Dept., METU

Asst. Dr. Cüneyt SERT
Mechanical Engineering Dept., METU

Dr. H. Tuğrul TINAZTEPE
Roketsan Missiles Industries Inc.

Date: 05.12.2008

I hereby declare that all information in this document has been obtained and presented in accordance with academic rules and ethical conduct. I also declare that, as required by these rules and conduct, I have fully cited and referenced all material and results that are not original to this work.

Name, Last name : Mustafa Emre BOYSAN

Signature :

ABSTRACT

ANALYSIS OF REGENERATIVE COOLING IN LIQUID PROPELLANT ROCKET ENGINES

BOYSAN, Mustafa Emre

M. Sc., Department of Mechanical Engineering

Supervisor: Assoc. Prof. Dr. Abdullah ULAŞ

December 2008, 82 pages

High combustion temperatures and long operation durations require the use of cooling techniques in liquid propellant rocket engines. For high-pressure and high-thrust rocket engines, regenerative cooling is the most preferred cooling method. In regenerative cooling, a coolant flows through passages formed either by constructing the chamber liner from tubes or by milling channels in a solid liner. Traditionally, approximately square cross sectional channels have been used. However, recent studies have shown that by increasing the coolant channel height-to-width aspect ratio and changing the cross sectional area in non-critical regions for heat flux, the rocket combustion chamber gas side wall temperature can be reduced significantly without an increase in the coolant pressure drop.

In this study, the regenerative cooling of a liquid propellant rocket engine has been numerically simulated. The engine has been modeled to operate on a

LOX/Kerosene mixture at a chamber pressure of 60 bar with 300 kN thrust and kerosene is considered as the coolant. A numerical investigation was performed to determine the effect of different aspect ratio cooling channels and different number of cooling channels on gas-side wall and coolant temperature and pressure drop in cooling channel.

Key-words: Liquid Propellant Rocket Engines, Regenerative Cooling, Cooling Efficiency, Cooling Channel, Liquid Oxygen, Kerosene.

ÖZ

SIVI YAKITLI ROKET MOTORLARINDA REJENERATİF SOĞUTMA ANALİZLERİ

BOYSAN, Mustafa Emre

Yüksek Lisans, Makina Mühendisliği Bölümü

Tez Yöneticisi: Doç. Dr. Abdullah ULAŞ

Aralık 2008, 82 sayfa

Yüksek yanma sıcaklıkları ve uzun çalışma süreleri, sıvı yakıtlı roket motorlarında soğutma tekniklerinin kullanılmasını gerekli kılar. Yüksek basınçlı ve yüksek itkili roket motorlarında rejeneratif soğutma, öncelikli tercih edilen soğutma tekniklerinden biridir. Rejeneratif soğutma, soğutma akışkanının yanma odası duvarlarına yerleştirilen tüplerden veya yanma odası duvarlarına işlenen kanallardan geçirilmesiyle sağlanır. Soğutma kanalları için genellikle kare kesit alanları tercih edilmekteyken, yapılan çalışmalarda kanal kesit alanlarında yükseklik genişlik oranının artırılmasıyla ve ısı akısı bakımından kritik olmayan bölgelerde kesit alanlarının değiştirilmesiyle, kanal içinde basınç düşüşünü çok etkilemeden yanma odası iç yüzeyindeki sıcaklık değerlerinin düşürülebildiği gösterilmiştir.

Bu alıřmada, sıvı yakıtlı roket motorlarında kullanılan sođutma kanalları hesaplamalı akıřkanlar dinamiđi ile benzeřtirilmiřtir. Motor, sıvı oksijen ve kerosen karıřımı ile 60 bar yanma odası basıncı ve 300 kN'luk itki seviyesini oluřturacak řekilde tasarlanmıř, sođutma akıřkanı olarak kerosen seilmiřtir. Hesaplamalı akıřkanlar dinamiđi ile farklı ykseklik-geniřlik oranları ve kullanılan kanal sayılarının, yanma odası i yzeyinin ve sođutma akıřkanının sıcaklık deđerlerine ve kanal ii basın dřřne etkileri incelenmiřtir.

Anahtar Kelimeler: Sıvı Yakıtlı Roket Motorları, Yanma Odası, Regeneratif Sođutma, Sođutma Verimliliđi, Sođutma Kanalları, Sıvı Oksijen, Kerosen.

ACKNOWLEDGEMENTS

I am extremely grateful to my supervisor Assoc. Prof. Dr. Abdullah ULAŞ for his professional support, guidance and encouragement throughout the completion of this thesis work. I deeply appreciate his patience and many efforts to proofread my thesis over and over again.

I would like to express my sincere appreciation to my colleagues Bora KALPAKLI for his crucial advises, Ezgi CİVEK and Göktuğ KARACALIOĞLU for their invaluable efforts during the preparation of this thesis.

I would like to thank to Dr. Tuğrul TINAZTEPE, Başar SEÇKİN and Dr. Atılğan TOKER for their great support and encouragement and ROKETSAN for partially supporting this study.

Love and thanks to my family, my flat mates and my friends for their never-ending patience, support and encouragement.

Ankara, December 2008

Mustafa Emre Boysan

TABLE OF CONTENTS

ABSTRACT	IV
ÖZ	VI
ACKNOWLEDGEMENTS	VIII
TABLE OF CONTENTS	IX
LIST OF TABLES	XI
LIST OF FIGURES	XIII
LIST OF SYMBOLS	XVI
1 INTRODUCTION	1
2 BACKGROUND	4
2.1 REGENERATIVE COOLING	4
2.2 SELECTION OF COOLING PASSAGES GEOMETRY	6
2.3 SELECTION OF MATERIALS FOR THRUST CHAMBERS.....	7
2.4 HEAT TRANSFER ANALYSIS.....	8
2.4.1 <i>Definition of the Problem</i>	9
2.4.2 <i>Gas Side Heat Transfer</i>	10
2.4.3 <i>Coolant Side Heat Transfer</i>	13
2.4.4 <i>Pressure Drop in Cooling Channels</i>	16
3 MATHEMATICAL DESCRIPTION AND SOLUTION METHOD	18
3.1 MATHEMATICAL DESCRIPTION.....	18
3.2 SOLUTION METHOD.....	21
3.2.1 <i>Thermochemical Equilibrium Code</i>	22
3.2.2 <i>User Defined Function for Solver</i>	22
3.2.3 <i>Grid Generator and Solver</i>	22
4 VALIDATION	23

4.1	BASILINE SOLUTION	25
4.1.1	<i>Grid Generation</i>	25
4.1.2	<i>Material Properties</i>	26
4.1.3	<i>Results and Discussion</i>	26
4.2	BIFURCATION CHANNEL SOLUTION.....	29
4.3	DISCUSSION	30
5	THRUST CHAMBER PRELIMINARY DESIGN.....	31
5.1	NOZZLE CONTOUR ESTIMATION FOR REGION II	35
5.2	LENGTH ESTIMATION FOR REGION I.....	37
5.3	NOZZLE CONTOUR ESTIMATION FOR REGION III.....	38
5.4	NOZZLE CONTOUR FOR THE DESIGNED THRUST CHAMBER.....	38
6	ANALYSIS AND RESULTS	39
6.1	MATERIAL PROPERTIES	39
6.2	BOUNDARY CONDITIONS	39
6.3	EFFECT OF RADIATION HEAT TRANSFER ON TEMPERATURE AND PRESSURE.....	41
6.4	EFFECT OF CHANNEL GEOMETRY ON COOLING EFFICIENCY	45
6.5	EFFECT OF NUMBER OF CHANNELS ON COOLING EFFICIENCY.....	56
6.6	COOLING CHANNELS WITH VARIABLE CROSS SECTION AREA.....	61
7	CONCLUSION AND DISCUSSION	67
	REFERENCES.....	69
	APPENDICES.....	73
A.	THERMAL PROPERTIES OF MATERIALS	73
B.	USER DEFINED FUNCTION FOR HEAT FLUX ON GAS SIDE WALL	79

LIST OF TABLES

Table 2.1 – Regeneratively Cooled Liquid Propellant Rocket Engines	4
Table 2.2 – Heat Transfer Characteristics of Several Liquid Propellants [3].....	15
Table 3.1 – Conservation Equation Variables	19
Table 4.1 – 89 kN GH ₂ and LOX Engine Specifications.....	24
Table 4.2 – Grid Specifications	25
Table 4.3 – Results of Baseline Solution	28
Table 4.4 – Comparison of Pressure Values	29
Table 5.1 – LPRE Requirements.....	32
Table 5.2 – Flame Temperatures and I _{sp} Values for Different O/F	32
Table 5.3 – Typical Characteristic Lengths for Various Propellant Combinations	36
Table 6.1 – Boundary Conditions for Inner Wall	40
Table 6.2 – Boundary Conditions for Outer Shell	41
Table 6.3 – Boundary Conditions for Coolant.....	41
Table 6.4 – Parameters for Radiation Heat Transfer Investigation.....	42
Table 6.5 – Results for Radiation Heat Transfer Investigation.....	43
Table 6.6 – Parameters for 4 mm Height Channels	46
Table 6.7 – Parameters for 8 mm Height Channels	46
Table 6.8 – Results for 4 mm Height Channels	47
Table 6.9 – Results for 8 mm Height Channels	47
Table 6.10 – Parameters for Number of Channels Investigation.....	56
Table 6.11 – Results for Channel Number Investigation.....	57
Table 6.12 – Results for Variable Cross Sectionx150 and 4x2x150	62
Table A.1 – Thermal Properties of Kerosene	73
Table A.2 – Thermal Properties of Liquid Hydrogen.....	75

Table A.3 – Thermal Properties of OFHC Copper	77
Table A.4 – Thermal Properties of INCONEL 718	78

LIST OF FIGURES

Figure 2.1 – Cross-Sectional View of a Thrust Chamber along Axial Direction with Regenerative Cooling.....	5
Figure 2.2 – Schematic Views for Dual Regenerative Cooling.....	5
Figure 2.3 – Cross-Sectional View for Different Type of Coolant Passages	6
Figure 2.4 – Typical Heat Flux Distribution along Thrust Chamber Wall.....	9
Figure 2.5 – Heat Transfer Schematic for Regenerative Cooling [1]	10
Figure 2.6 – Regimes in Transferring Heat from a Hot Wall to a Flowing Liquid [1]	14
Figure 3.1 – Schematic View of Solution Domain	18
Figure 3.2 – Convection and Radiation Heat Transfer from Combusted Gases to the Solution Domain	20
Figure 3.3 – Schematic View of Solution Method	21
Figure 4.1 – 89 kN GH ₂ and LOX Engine [17]	23
Figure 4.2 – Cross-Sectional View of Solution Domains.....	26
Figure 4.3 – Convergence History of Temperature Rise	27
Figure 4.4 – Convergence History of Pressure Drop.....	27
Figure 4.5 – Temperature Distribution on Gas Side Wall for Baseline Solution ...	28
Figure 4.6 – Temperature Distribution on Gas-Side Wall for Bifurcation Channel Solution.....	29
Figure 5.1 – The Scheme of LPRE Chamber.....	31
Figure 5.2 – Flame Temperature vs Mass Percentage of RP-1.....	33
Figure 5.3 – I _{sp} vs Mass Percentage of RP-1	33
Figure 5.4 – Calculated Combustion Chamber and Nozzle Contour for 300 kN LPRE.....	38

Figure 6.1 – Schematic View of Solution Domain	40
Figure 6.2 – Heat Flux Distribution on Gas Side Wall along Axial Direction for Radiation Heat Transfer Investigation	43
Figure 6.3 – Temperature Distribution on Gas Side Wall along Axial Direction for Radiation Heat Transfer Investigation	44
Figure 6.4 – Temperature Distribution of Coolant on Coolant Side Wall along Axial Direction for Radiation Heat Transfer Investigation	44
Figure 6.5 – Pressure Distribution of Coolant along Axial Direction for Radiation Heat Transfer Investigation.....	45
Figure 6.6 – Velocity Profiles of Coolant at Throat (x=0)	48
Figure 6.7 – Heat Flux Distribution on Gas Side Wall along Axial Direction for 4 mm Channel Height	49
Figure 6.8 – Heat Flux Distribution on Gas Side Wall along Axial Direction for 8 mm Channel Height	50
Figure 6.9 – Temperature Distribution on Gas Side Wall along Axial Direction for 4mm Channel Height	50
Figure 6.10 – Temperature Distribution on Gas Side Wall along Axial Direction for 8 mm Channel Height	51
Figure 6.11 – Temperature Distribution of Coolant on Coolant Side Wall along Axial Direction for 4 mm Channel Height.....	51
Figure 6.12 – Temperature Distribution of Coolant on Coolant Side Wall along Axial Direction for 8mm Channel Height.....	52
Figure 6.13 – Effects of Aspect Ratio on Gas Side Wall Temperature	53
Figure 6.14 – Effects of Aspect Ratio on Coolant Temperature.....	53
Figure 6.15 – Effects of Aspect Ratio on Pressure Drop in Channel	54
Figure 6.16 – Pressure Distribution of Coolant along Axial Direction for 4 mm Channel Height	55
Figure 6.17 – Pressure Distribution of Coolant along Axial Direction for 8 mm Channel Height	55
Figure 6.18 – Velocity Profiles of Coolant at Throat (x=0)	57
Figure 6.19 – Effects of Number of Channels on Gas Side Wall Temperature.....	58

Figure 6.20 – Effects of Number of Channels on Coolant Temperature	58
Figure 6.21 – Heat Flux Distribution on Gas Side Wall along Axial Direction for Different Number of Cooling Channels.....	59
Figure 6.22 – Temperature Distribution on Gas Side Wall along Axial Direction for Different Number of Cooling Channels.....	59
Figure 6.23 – Temperature Distribution of Coolant on Coolant Side Wall along Axial Direction for Different Number of Cooling Channels	60
Figure 6.24 – Effects of Number of Channels on Pressure Drop	60
Figure 6.25 – Pressure Distribution of Coolant along Axial Direction for Different Number of Channels	61
Figure 6.26 – Channel Geometry for Variable Cross Section Area	62
Figure 6.27 – Velocity Profiles of Coolant for Variable Cross Section Channel at Different Locations	63
Figure 6.28 – Temperature Distribution on Gas Side Wall along Axial Direction for 8 mm Channel Height	64
Figure 6.29 – Temperature Distribution of Coolant on Coolant Side Wall along Axial Direction for Variable Cross Section Area Investigation	64
Figure 6.30 – Pressure Distribution of Coolant along Axial Direction for Variable Cross Section Area Investigation.....	65
Figure A.1 – Temperature Variable C_p for Kerosene	73
Figure A.2 – Temperature Variable Thermal Conductivity for Kerosene.....	74
Figure A.3 – Temperature Variable Viscosity for Kerosene	74
Figure A.4 – Temperature Variable C_p for Liquid Hydrogen.....	75
Figure A.5 – Temperature Variable Thermal Conductivity for Liquid Hydrogen .	76
Figure A.6 – Temperature Variable Viscosity for Liquid Hydrogen.....	76
Figure A.7 – Temperature Variable C_p for OFHC Copper	77
Figure A.8 – Temperature Variable Thermal Conductivity for OFHC Copper	77
Figure A.9 – Temperature Variable C_p for INCONEL 718.....	78
Figure A.10 – Temperature Variable Thermal Conductivity for INCONEL 718 ..	78

LIST OF SYMBOLS

A	Area [m ²]
C*	Characteristic Velocity [m/s]
C ₁	Constant in turbulence Model
C ₂	Constant in turbulence Model
C _f	Thrust Coefficient
C _μ	Constant in turbulence Model
C _p	Specific Heat at Constant Pressure [J/kg-K]
d	Diameter [m]
D _h	Hydraulic Diameter [m]
f	Friction Factor
h	Heat Transfer Coefficient [W/m ² -K]
h	Height of Cooling Channel [mm]
I _{sp}	Specific Impulse [s]
k	Thermal Conductivity [W/m-K]
L	Length of Cooling Channel in Axial Direction [m]
m	Mass Flow Rate [kg/s]
M	Mach Number
n	Normal Outward Direction
P	Pressure [bar]
Pr	Prantl Number
q̇	Heat Flux [W/m ²]
r	Recovery Factor

Re	Reynolds Number
S	Source Term
T	Temperature [K]
u	Velocity Along x Direction [m/s]
v	Velocity Along y Direction [m/s]
V	Velocity Magnitude [m/s]
w	Width of Cooling Channel [mm]
ω	Velocity Along z Direction [m/s]
x	x axis of Cartesian Coordinate
y	y axis of Cartesian Coordinate
z	z axis of Cartesian Coordinate

Other Symbols:

σ_{κ}	Turbulent Prandtl Numbers for κ
σ_{ε}	Turbulent Prandtl Numbers for ε
σ_T	Turbulent Prandtl Numbers for T
ρ	Density [kg/m ³]
γ	Specific Heat Ratio
μ	Viscosity [kg/m-s]
μ_{eff}	Effective Turbulence Viscosity [kg/m-s]
μ_t	Turbulence Viscosity [kg/m-s]

Subscripts:

aw	Adiabatic Wall Temperature
c	Chamber
cb	Coolant Bulk Temperature
conv.	Convection

CO ₂	Carbon Dioxide
H ₂ O	Water Vapor
g	Gas Domain
l	Liquid Domain
ox	Oxidizer
pr	Propellant
rad.	Radiation
s	Solid Domain
t	Throat
tot	Total
wc	Coolant Side Wall
wg	Gas Side Wall

CHAPTER 1

INTRODUCTION

All rocket engines have one problem in common; high energy released by combusted gases. This problem results in high combustion temperatures (2400 to 3600 K), high heat transfer rates (0.8 to 160 MW/m²) in thrust chamber and requires special cooling techniques for the engine [1]. Cooling techniques developed to cope with this problem, either singly or in combination, include regenerative cooling, radiation cooling, film or transpiration cooling, ablation, and inert or endothermic heat sinks [2]. To choose the proper cooling technique mission requirements, environmental requirements and operational requirements should be considered.

Regenerative cooling is one of the most widely applied cooling techniques used in liquid propellant rocket engines [1]. It has been effective in applications with high chamber pressure and for long durations with a heat flux range 1.6 to 160 MW/m² [3].

Regenerative cooling of a liquid propellant rocket engine consists of a balance between the energy rejected by the combusted gases and the heat energy absorbed by the coolant [4]. The energy absorbed by the coolant is not wasted; it augments the initial energy content of the propellant prior to injection, increasing the exhaust velocity slightly (0.1 to 1.5%) [2]. Therefore thermal energy is recovered in the

system [5]. However by this process the overall engine performance gain is less than 1% [1].

Basically there are three domains in a regeneratively cooled rocket engine; gas domain (combusted gases), liquid domain (coolant) and the solid domain (thrust chamber wall). The heat transfer analysis in regenerative cooling are simply based on convection and radiation heat transfer for gas domain, conduction heat transfer for solid domain and convection heat transfer for liquid domain. Heat transfer from the outer surface of thrust chamber to the environment can be neglected and the outer surface wall can be assumed as adiabatic [6]. To simplify the gas side and coolant side heat transfer analysis, many correlations are developed to calculate the heat transfer coefficients.

In this study, the effects of geometry and number of rectangular cooling channels on cooling efficiency are investigated in terms of the maximum temperature of thrust chamber wall and coolant, and the pressure drop in cooling channel.

Thrust chamber is geometry is obtained preliminary according to the design parameters that are determined for future works. Thermal properties of combustion gases are calculated with thermochemical equilibrium code [7]. The contour of thrust chamber is obtained by using isentropic gas equations [8, 9] and nozzle contour design tools [10, 11].

Heat transfer analysis from gas side domain (combustion gases) to the solid domain (thrust chamber) is simulated with Bartz correlation [12]. Therefore solution domain consists of only liquid domain (coolant) and solid domain (thrust chamber wall).

GAMBIT [13] and FLUENT [14] software programs are used as grid generator and solver respectively in the solution. Fluid flow in the cooling channel is assumed to

be three-dimensional, steady-state and turbulent. The standard k- ϵ turbulence model is employed to the model [15].

Solution method is validated with experimental and numerical studies [16, 17]. The effect of radiation heat transfer on temperature and pressure values of the system is investigated. Several different channel geometries are formed with different constant cross-section area in axial direction and analyses are performed. Results are examined according to the maximum temperature of thrust chamber wall and coolant, and also pressure drop in cooling channel. The most suitable geometry from the engineering point of view is selected and optimum number of cooling channel is found for this geometry with additional analyses. To decrease the pressure drop in the cooling channel, cross-section area is increased in non-critical regions, final analysis is performed and final geometry is obtained.

CHAPTER 2

BACKGROUND

2.1 Regenerative Cooling

Regenerative cooling is first demonstrated in 1938 in United States by James H. Wyld [18] and today one of the most widely applied cooling technique used in liquid propellant rocket engines. Some of the engines, which use regenerative cooling, and their specifications is given in Table 2.1.

Table 2.1 – Regeneratively Cooled Liquid Propellant Rocket Engines

Rocket	Country	Thrust [N]	Chamber Pressure [bar]	Oxidizer	Fuel
AETUS II	Germany	30,000	10	NTO	MMH
RL10A	USA	64,700	40	LOX	LH ₂
RD861K	Ukraine	77,600	90	NTO	UDMH
VINCI	Germany	155,000	60	LOX	LH ₂
FASTRAC	USA	270,000	80	LOX	Kerosene
HM7B	France	-	35	LOX	LH ₂

In regenerative cooling process, the coolant, generally the fuel enters passages at nozzle exit of the thrust chamber, passes by the throat region and exits near the injector face. Cross-sectional view of a regeneratively cooled thrust chamber along the rocket axis is given in Figure 2.1.

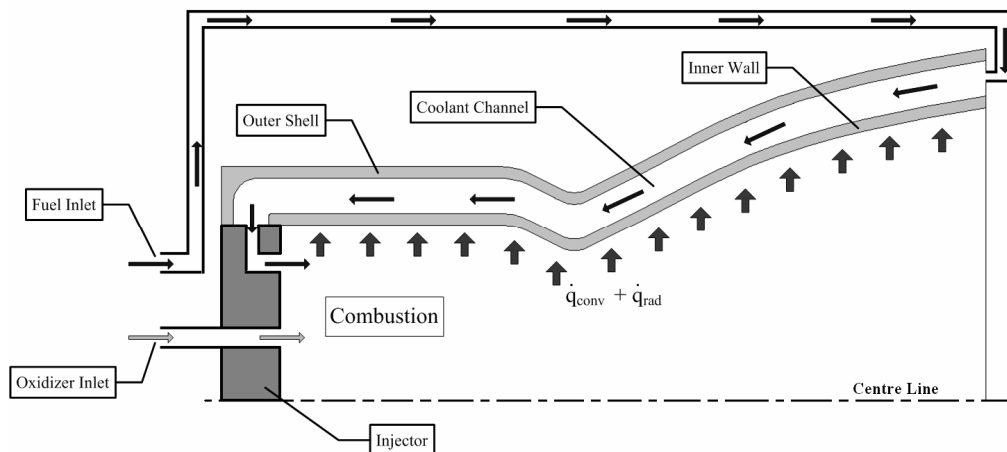


Figure 2.1 – Cross-Sectional View of a Thrust Chamber along Axial Direction with Regenerative Cooling

The nozzle throat region usually has the highest heat flux and is therefore the most difficult to cool. For this reason the cooling passage is often designed so that the coolant velocity is highest at the critical regions by restricting the coolant passage cross-section [3]. In some cases to increase the cooling efficiency, coolant can enter the coolant passages either from the nozzle exit and throat (Figure 2.2-a) or directly from the throat (Figure 2.2-b). This type of regenerative cooling is called as dual regenerative cooling [19].

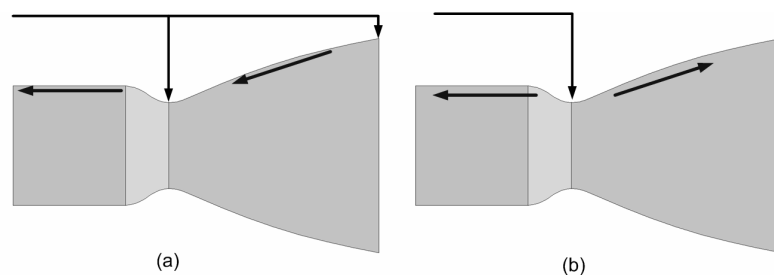


Figure 2.2 – Schematic Views for Dual Regenerative Cooling

2.2 Selection of Cooling Passages Geometry

Mainly two types of cooling techniques are used in regenerative cooling. Cooling passages can consist of an assembly of contoured adjacent tubes or separate inner wall.

In the first technique cooling tubes are brazed together to an outer shell that forms the contour of thrust chamber. In this technique the cross-sectional area of the tubes are changed according to the region of thrust chamber. For the high heat flux regions, tubes are elongated and squeezed to increase the velocity of the coolant and to increase the heat transfer area (Figure 2.3.a-b).

In the second technique, rectangular cooling channels are milled along the contour of a relatively thick thrust chamber. The cross-sections of the rectangular passages are smaller in the high heat flux regions to increase the velocity of the coolant. Outer shell is added to enclose the cooling passages (Figure 2.3.c).

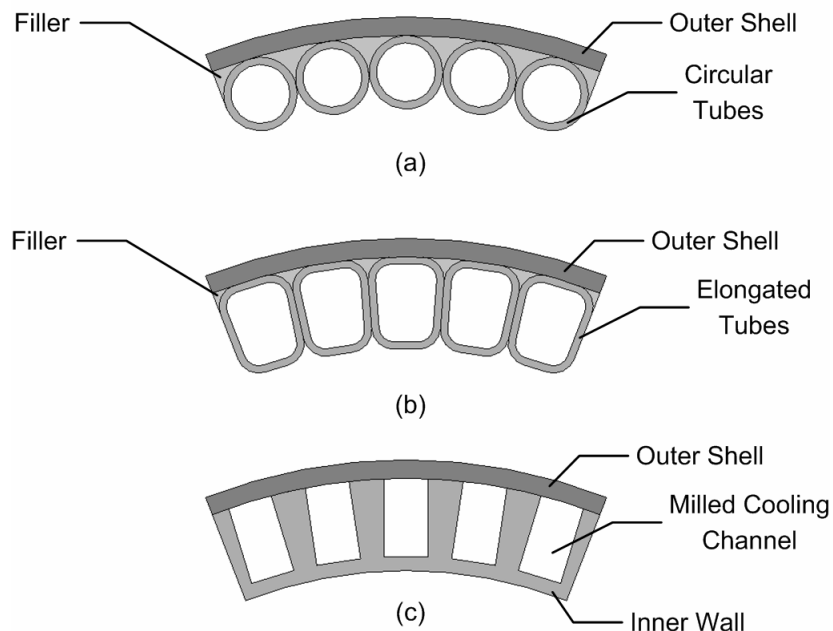


Figure 2.3 – Cross-Sectional View for Different Type of Coolant Passages

In 1990, by conventional manufacturing techniques, aspect ratios (ratio of channel height to channel width) as high as 8 could be manufactured and by introducing the platelet technology [20] aspect ratio of cooling channels is increased as high as 15. Today, improvements in manufacturing technologies have shown that by conventional manufacturing methods (milling), cooling channels with an aspect ratio 16 (8 mm height and 0.5 mm width) can be milled [21].

2.3 Selection of Materials for Thrust Chambers

The material selection for the brazed tubes or inner wall depends on the amount of the heat flux and coolant properties. For most applications, copper is used for tubes and inner wall. Copper is an excellent conductor and does not oxidize in fuel rich non-corrosive gas mixtures [3]. To increase the strength of material, copper alloys with small additions of zirconium, silver or silicon can be used for thrust chambers. Amzirc and NARloy-Z are two examples for copper alloys used for thrust chambers.

Amzirc is a copper base alloy containing nominal 0.15 % zirconium. This zirconium copper alloy combines high electrical and thermal conductivity with good strength retention at high temperatures. NARloy-Z is a copper base alloy containing a nominal 3 % silver and 0.5 % zirconium. The silver zirconium copper alloy combines high electrical and thermal conductivity with moderate strength retention at high temperatures [22]. Although these materials have better strength retention, they have lower conductivity than oxygen free high conductivity (OFHC) copper.

For propellant combinations with corrosive and aggressive oxidizers (nitric acid or nitrogen tetroxide) stainless steel is used as the inner wall material, since copper would chemically react with these propellants [3].

Nickel and nickel alloys are preferred for the thrust chamber outer shell. INCONEL-718 is a nickel chromium base alloy used in aircraft turbojet engines, thrust chamber outer shells, bellows and tubing for liquid oxygen type rocket engines [23]. INCONEL-718 has high yield, tensile, creep and creep-rupture strength at high temperatures up to 1000 K and at cryogenic temperatures [23].

2.4 Heat Transfer Analysis

In actual rocket development, not only the heat transfer is analyzed but also the rocket units are almost always tested to assure that the heat is transferred satisfactorily under all operating and emergency conditions. Heat transfer analysis is required to guide the design, testing and failure investigations [3].

Several different computational fluid dynamics (CFD) computer programs have been used for the analysis of thrust chamber steady-state heat transfer, with different chamber geometries or different materials with temperature variable properties. Some of the computer programs are described below.

Rocket thermal evaluation (RTE) code and two-dimensional kinetics nozzle performance code (TDK) are developed for the analysis of liquid propellant rocket engines with regenerative cooling by NASA. RTE is a three dimensional analysis code and uses a three dimensional finite differencing method. A Gauss-Seidel iterative method is used at each axial location to determine the wall temperature distributions. Gas properties (GASP) and complex chemical equilibrium and transport properties (CAT) are the two subroutines used in this code to determine the coolant and hot-gas-side thermal properties. TDK code evaluates the heat fluxes on hot-gas-side walls with the wall temperature distribution from RTE. Chamber pressure, coolant temperature, mass flow rates and coolant inlet pressure are given as input parameters; pressure drop, hot-gas-side wall temperature and coolant exit pressure are the results of the solution [16, 17, 19, 24].

GEMS (general equation and mesh solver) solves the conservation equations for an arbitrary material using a hybrid structured/unstructured grid developed by Purdue University. The code divides the computational domain into several zones where in each zone different types of conservation equations can be described [6].

Rocket engine heat transfer evaluation computer code (REHTEP) [20] calculates the gas side and coolant side heat transfer coefficients with basic correlations for rocket engines and this data is imported into a two-dimensional conduction analysis which used a numerical differencing analyzer computer program (SINDA) [20, 25]; developed by NASA; to calculate the wall temperature profiles.

2.4.1 Definition of the Problem

Only 0.5 to 5 % of total energy generated by combustion is transmitted to all internal surfaces of thrust chamber exposed to hot gases [3]. Local heat flux values vary along the thrust chamber wall according to geometry and design parameters of thrust chamber. A typical heat flux distribution along the thrust chamber wall is given in Figure 2.4. The peak is always at the nozzle throat and the lowest value is usually near the nozzle exit for uncooled thrust chambers.

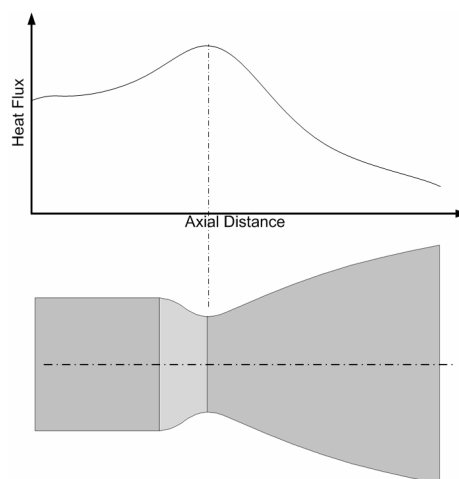


Figure 2.4 – Typical Heat Flux Distribution along Thrust Chamber Wall

Heat transfer in a regeneratively cooled chamber can be described as the heat flow between two moving fluids, through a multilayer partition as given in Figure 2.5 and total heat flux can be given as:

$$\dot{q}_{\text{tot}} = \dot{q}_g = \dot{q}_s = \dot{q}_c \quad (2.1)$$

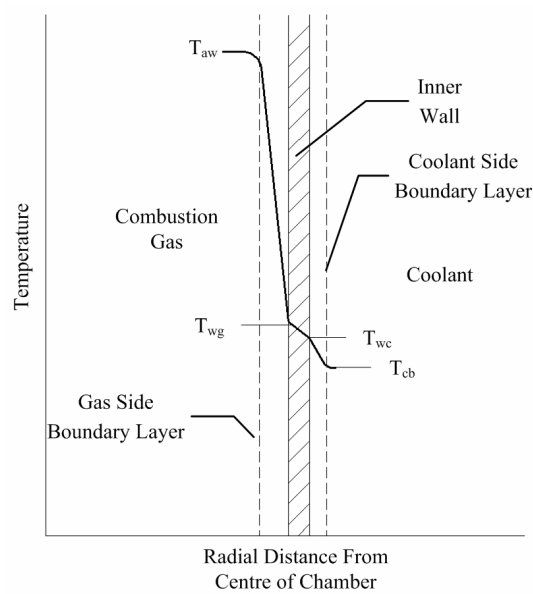


Figure 2.5 – Heat Transfer Schematic for Regenerative Cooling [1]

2.4.2 Gas Side Heat Transfer

The heat transfer between the combusted gases and thrust chamber wall is by convection and radiation.

$$\dot{q}_g = \dot{q}_{g,\text{conv}} + \dot{q}_{g,\text{rad}} \quad (2.2)$$

2.4.2.1 Heat Transfer by Convection

In thrust chamber, before the combusted gases can transfer heat to the wall, the heat energy must pass through a layer of stagnant gas along the wall, boundary

layer. This basic correlation for this complicated convective heat transfer can be expressed by the following equation:

$$\dot{q}_{g,conv} = h_g (T_{aw} - T_{wg}) \quad (2.3)$$

The adiabatic wall temperature of combustion gas at a given location in the thrust chamber may be obtained from the following expression:

$$T_{aw} = T_c \left[\frac{1 + r \left(\frac{\gamma - 1}{2} \right) M^2}{1 + \left(\frac{\gamma - 1}{2} \right) M^2} \right] \quad (2.4)$$

where recovery factor (r) can be estimated for turbulent flows as:

$$r = (\text{Pr})^{0.33} \quad (2.5)$$

Determination of gas side heat transfer coefficient presents a very complex problem. Comparisons of analytical results with experimental heat transfer data have often shown disagreement. The differences are largely attributed to the initial assumptions for analytical calculations. The boundary layer that controls the heat transfer rate to the wall is greatly affected by the turbulent combustion process, local gas compositions and temperature. Also each injector configuration produces different combustion [1].

Based on experience with turbulent boundary layer, some relatively simple correlations for the calculation of gas side heat transfer have been developed.

Bartz Correlation [12] is a well known equation used for estimation of rocket nozzle convective heat transfer coefficients based on thermal properties of

combusted gases and isentropic gas equations. In this study and also in references [26] and [27], heat transfer coefficient is estimated in terms of gas side wall temperature by using Bartz Correlation.

$$h_g = \frac{0.026}{d_t^{0.2}} \left(\frac{\mu_g^{0.2} C_{p,g}}{\text{Pr}_g^{0.6}} \right)_0 \left(\frac{P_c}{C^*} \right)^{0.8} \left(\frac{A_t}{A} \right)^{0.9} \sigma \quad (2.6)$$

$$\sigma = \left[0.5 \frac{T_{wg}}{T_c} \left(1 + \frac{\gamma-1}{2} M^2 \right) + 0.5 \right]^{-0.68} \left(1 + \frac{\gamma-1}{2} M^2 \right)^{-0.12} \quad (2.7)$$

Based on the experimental studies of Ciniaref and Dobrovolski [28] the relation for convective heat transfer can be given as:

$$h_g = \frac{k_g}{d} 0.0162 \text{Pr}_g^{0.82} \text{Re}_g^{0.82} \left(\frac{T_{aw}}{T_{wg}} \right)^{0.35} \quad (2.8)$$

2.4.2.2 Heat Transfer by Radiation

The exact solution of the amount of heat transmitted to the wall by radiation is an extremely complex problem for rocket propulsion systems.

In rocket combustion devices, gas temperature varies between 1900 and 3900 K; where radiation heat transfer of combusted gases contributes 3 to 40% of the heat transfer to the chamber walls, depending on the reaction gas composition, chamber size, geometry and temperature [3].

Gases with symmetrical molecules, such as hydrogen, oxygen, and nitrogen, have been found not to show many strong emission bands. Also they do not really absorb radiation and do not increase the radiation heat transfer. Heteropolar gases, such as water vapor, carbon monoxide, carbon dioxide and etc. have strong emission bands [3].

For the propellants containing only carbon, hydrogen, oxygen, and nitrogen atoms, the total radiation heat flux can be approximated as [29]:

$$\dot{q}_{g,rad} \approx \dot{q}_{rad,CO_2} + \dot{q}_{rad,H_2O} \quad (2.9)$$

$$\dot{q}_{rad,CO_2} = 3.5\sqrt[3]{P_{CO_2} L_e} \left[\left(\frac{T_{aw}}{100} \right)^{3.5} - \left(\frac{T_{wg}}{100} \right)^{3.5} \right] \quad (2.10)$$

$$\dot{q}_{rad,H_2O} = 3.5P_{H_2O}^{0.8} L_e^{0.6} \left[\left(\frac{T_{aw}}{100} \right)^3 - \left(\frac{T_{wg}}{100} \right)^3 \right] \quad (2.11)$$

where $L_e = 0.6D$ in [m], heat flux in [$\text{kcal}/\text{m}^2\text{-h}$] and pressure in [kg/cm^2].

2.4.3 Coolant Side Heat Transfer

The heat transfer between the coolant and thrust chamber wall is by forced convection.

$$\dot{q}_l = \dot{q}_{l,conv} \quad (2.12)$$

$$\dot{q}_{l,conv} = h_l(T_{wc} - T_{cb}) \quad (2.13)$$

The coolant side heat transfer coefficient is influenced by many factors. Propellants used for coolant may become corrosive, may decompose, or may deposit impurities under high temperatures and heat fluxes, thereby reducing cooling effectiveness. It is not possible to get the actual heat transfer coefficients without experiments [1].

The characteristic of coolant side heat transfer depend largely on the coolant pressure and coolant side wall temperature (Figure 2.6). Curve A indicates the behavior of heat transfer at coolant pressure below critical pressure. Line segment $A_1 - A_2$ represents the forced convection when the temperature of the coolant is

below critical temperature. As the wall temperature of the coolant increases and exceeds the critical temperature, small bubbles started to form in the boundary and grow continuously. When the bubbles reach the colder liquid stream, they condensate. This phenomenon is known as nucleate boiling and corresponds line segment $A_2 - A_3$ in Figure 2.6. Nucleate boiling increase the heat transfer coefficient, resulting in little increase in wall temperature for a wide range of heat flux. A further increase in the heat flux increase the bubble population, gas film occurs in the boundary and decrease heat transfer coefficient. Coolant side wall temperature increases so high and causes failure of the wall material. Therefore for coolant pressure values below critical temperature, A_3 is the maximum heat flux for nucleate boiling and used as a design criteria for regenerative cooling [1].

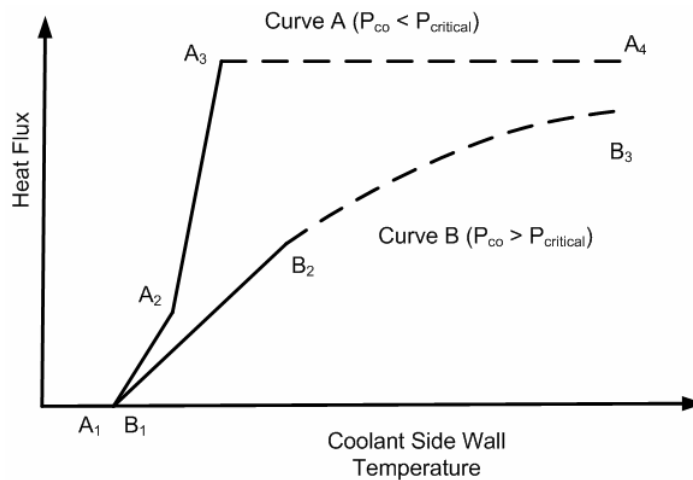


Figure 2.6 – Regimes in Transferring Heat from a Hot Wall to a Flowing Liquid [1]

Curve B indicates the heat transfer behavior of coolant for pressure levels above critical pressure. Since no boiling can occur, the wall temperature continuously increases as the heat flux increases and heat transfer coefficient remains essentially constant (line segment $B_1 - B_2$). If the wall temperature reaches and exceeds the critical temperature of coolant, a stable supercritical vapor-film boundary layer forms; this results in lower heat transfer coefficients and lower cooling efficiencies (line segment $B_2 - B_3$). Heat transfer can be increased up to the critical temperature

values of the wall material. Heat transfer characteristic of some propellants used for regenerative cooling is given in Table 2.2.

Table 2.2 – Heat Transfer Characteristics of Several Liquid Propellants [3]

Liquid Coolant	Boiling Characteristics			Nucleate Boiling Characteristics		
	Pressure [MPa]	Boiling Temp. [K]	Critical Temp. [K]	Critical Pressure [MPa]	Temp. [K]	Pressure [MPa]
Hydrazine	0.101	387	652	14.7	322.2	4.31
	0.689	455				
	3.45	540			405.6	4.31
	6.89	588				
Kerosene	0.101	490	678	2.0	297.2	0.689
	0.689	603				
	1.38	651			297.2	1.38
Nitrogen tetroxide	0.101	294	431	10.1	288.9	4.31
	0.689	342			322.2	
	4.31	394			366.7	
Unsymm. dimethyl hydrazine	0.101	336	522	6.06	300	2.07
	1.01	400				
	3.45	489			300	5.22

For the non-boiling subcritical regions (line segments $A_1 - A_2$ and $B_1 - B_2$), it is possible to predict the heat transfer coefficient. Some correlations are defined to calculate the heat transfer coefficient based on experimental studies.

The correlations used for coolant side heat transfer are principally based on the conventional Dittus-Boelter equation for turbulent, thermally fully developed flow for fluids with constant property values [30]. Some of the correlations used for regenerative cooling analysis are given below.

Ciniaref and Dobrovolski [28]:

$$\text{Nu} = \frac{h_1 D_h}{k_1} = 0.021 \text{Re}_1^{0.8} \text{Pr}_1^{0.43} \left(\frac{\text{Pr}_1}{\text{Pr}_{1,\text{wc}}} \right)^{0.25} \quad (2.14)$$

Taylor [31]:

$$\text{Nu} = \frac{h_1 D_h}{k_1} = 0.023 \text{Re}_1^{0.8} \text{Pr}_1^{0.4} \left(\frac{T_{\text{wc}}}{T_{\text{cb}}} \right)^{-\left(0.57 - 1.59 \frac{D_h}{x}\right)} \quad (2.15)$$

Sieder and Tate [32]:

$$\text{Nu} = \frac{h_1 D_h}{k_1} = 0.027 \text{Re}_1^{0.8} \text{Pr}_1^{0.33} \left(\frac{\mu_1}{\mu_{1,\text{cw}}} \right)^{-0.14} \quad (2.16)$$

McCarthy and Wolf [33]:

$$\text{Nu} = \frac{h_1 D_h}{k_1} = 0.025 \text{Re}_1^{0.8} \text{Pr}_1^{0.4} \left(\frac{T_{\text{wc}}}{T_{\text{cb}}} \right)^{-0.55} \quad (2.17)$$

2.4.4 Pressure Drop in Cooling Channels

A higher pressure drop allows a higher velocity in the coolant channel which increases the cooling efficiency but requires heavier feeding systems which decreases the system efficiency of the propulsion system.

The pressure drop in steady, laminar and fully-developed flow of an incompressible fluid through a horizontal pipe can be defined as [34]:

$$\Delta P = f \frac{L}{D_h} \frac{\rho V^2}{2} \quad (2.18)$$

CHAPTER 3

MATHEMATICAL DESCRIPTION AND SOLUTION METHOD

3.1 MATHEMATICAL DESCRIPTION

The solution domain used in this study consists of 3 medium: coolant, inner wall of the thrust chamber and outer shell of the thrust chamber. Because of the symmetry characteristic of the system, the domain is divided by two symmetry planes (Figure 3.1).

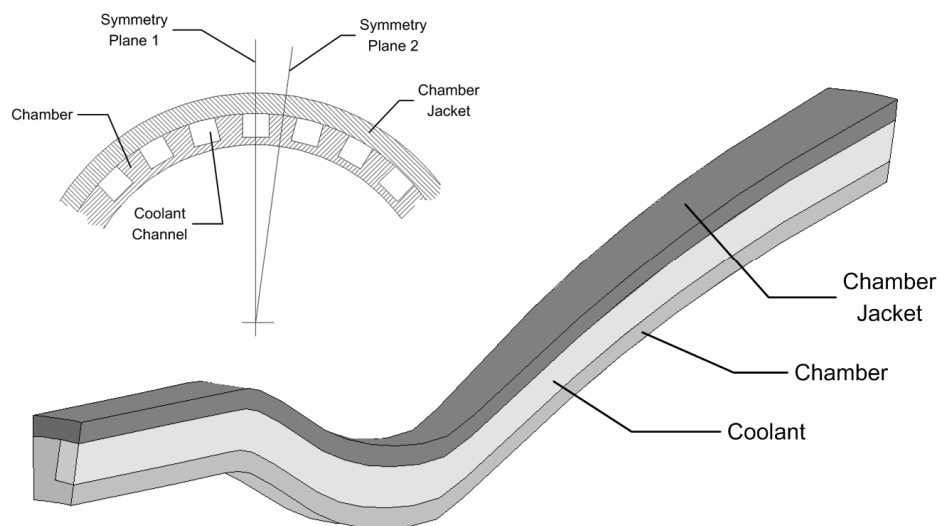


Figure 3.1 – Schematic View of Solution Domain

In this study the fluid flow and heat transfer in the cooling channel was assumed to be three-dimensional, steady-state and turbulent flow. The standard k-ε turbulence model is employed to the model. The conservation equations of fluid flow and heat transfer are expressed as:

$$\nabla \cdot (\rho \bar{V} \phi) = \nabla \cdot (\Gamma_\phi \nabla \phi) + S_\phi \quad (3.1)$$

where the expressions of ϕ , Γ_ϕ and S_ϕ for different variables are given in Table 3.1.

Table 3.1 – Conservation Equation Variables

Equations	ϕ	Γ_ϕ	S_ϕ		
Continuity Equation	1	0	0		
u Equation	u	μ_{eff}	$-\frac{\partial p}{\partial x} + \frac{\partial}{\partial x} \left(\mu_{\text{eff}} \frac{\partial u}{\partial x} \right) + \frac{\partial}{\partial y} \left(\mu_{\text{eff}} \frac{\partial v}{\partial x} \right) + \frac{\partial}{\partial z} \left(\mu_{\text{eff}} \frac{\partial \omega}{\partial x} \right)$		
v Equation	v	μ_{eff}	$-\frac{\partial p}{\partial y} + \frac{\partial}{\partial x} \left(\mu_{\text{eff}} \frac{\partial u}{\partial y} \right) + \frac{\partial}{\partial y} \left(\mu_{\text{eff}} \frac{\partial v}{\partial y} \right) + \frac{\partial}{\partial z} \left(\mu_{\text{eff}} \frac{\partial \omega}{\partial y} \right)$		
ω Equation	ω	μ_{eff}	$-\frac{\partial p}{\partial z} + \frac{\partial}{\partial x} \left(\mu_{\text{eff}} \frac{\partial u}{\partial z} \right) + \frac{\partial}{\partial y} \left(\mu_{\text{eff}} \frac{\partial v}{\partial z} \right) + \frac{\partial}{\partial z} \left(\mu_{\text{eff}} \frac{\partial \omega}{\partial z} \right)$		
Energy Equation	T	$\mu/\text{Pr} + \mu/\sigma_T$	0		
k Equation	k	$\mu + (\mu/\sigma_k)$	$\rho G_k - \rho \varepsilon$		
ε Equation	ε	$\mu + (\mu/\sigma_\varepsilon)$	$\frac{\varepsilon}{k} (C_1 \rho G_k - C_2 \rho \varepsilon)$		
$G_k = \left(\frac{\mu_t}{\rho} \right) \left[\left(\frac{\partial u}{\partial x} \right)^2 + \left(\frac{\partial \omega}{\partial y} \right)^2 + \left(\frac{\partial \omega}{\partial z} \right)^2 \right] + \left[\left(\frac{\partial u}{\partial y} \right) + \left(\frac{\partial v}{\partial x} \right) \right]^2 + \left[\left(\frac{\partial u}{\partial z} \right) + \left(\frac{\partial \omega}{\partial x} \right) \right]^2 + \left[\left(\frac{\partial v}{\partial z} \right) + \left(\frac{\partial \omega}{\partial y} \right) \right]^2$					
$C_\mu = 0.09$	$C_1 = 1.44$	$C_2 = 1.92$	$\sigma_k = 1.0$	$\sigma_\varepsilon = 1.3$	$\sigma_T = 0.85$

The effect of heat transfer from combusted gases to the solution domain is considered in two parts: convection heat transfer and radiation heat transfer as shown in Figure 3.2.

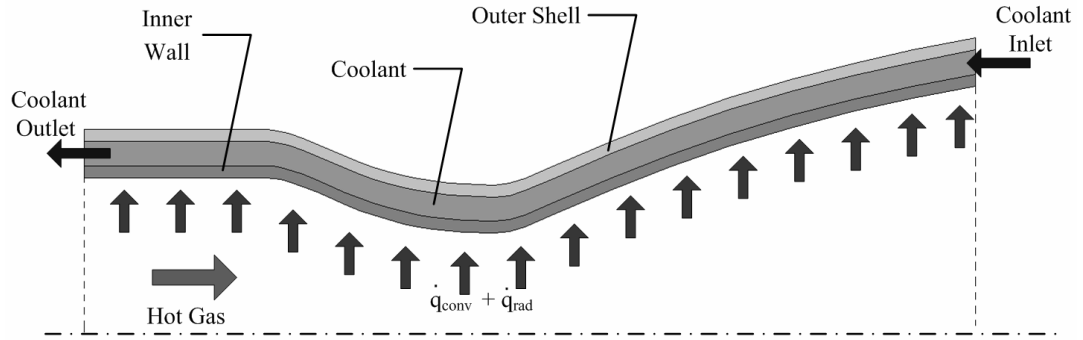


Figure 3.2 – Convection and Radiation Heat Transfer from Combusted Gases to the Solution Domain

Convection heat flux can be given as:

$$\dot{q}_{\text{conv}} = h_g (T_{\text{aw}} - T_{\text{wg}}) \quad (3.2)$$

Heat transfer coefficient can be calculated by using Bartz Correlation [13] as:

$$h_g = \frac{0.026}{d_t^{0.2}} \left(\frac{\mu_c^{0.2} C_{p,c}}{\text{Pr}_c^{0.6}} \right) \left(\frac{P_c}{C^*} \right)^{0.8} \left(\frac{A_t}{A} \right)^{0.9} \sigma \quad (3.3)$$

$$\sigma = \left[0.5 \frac{T_{\text{wg}}}{T_c} \left(1 + \frac{\gamma-1}{2} M^2 \right) + 0.5 \right]^{-0.68} \left(1 + \frac{\gamma-1}{2} M^2 \right)^{-0.12} \quad (3.4)$$

$$T_{\text{aw}} = T_c \left[\frac{1 + r \left(\frac{\gamma-1}{2} \right) M^2}{1 + \left(\frac{\gamma-1}{2} \right) M^2} \right] \quad (3.5)$$

where $r = (\text{Pr}_c)^{0.33}$ for turbulent flows.

For the propellants containing only carbon, hydrogen, oxygen, and nitrogen atoms, the total radiation heat flux, can be approximated as [28]:

$$\dot{q}_{\text{rad}} \approx \dot{q}_{\text{rad,CO}_2} + \dot{q}_{\text{rad,H}_2\text{O}} \quad (3.6)$$

$$\dot{q}_{\text{rad,CO}_2} = 3\sqrt[3]{p_{\text{CO}_2} L_e} \left[\left(\frac{T_{\text{aw}}}{100} \right)^{3.5} - \left(\frac{T_{\text{wg}}}{100} \right)^{3.5} \right] \quad (3.7)$$

$$\dot{q}_{\text{rad,H}_2\text{O}} = 3p_{\text{H}_2\text{O}}^{0.8} L_e^{0.6} \left[\left(\frac{T_{\text{aw}}}{100} \right)^3 - \left(\frac{T_{\text{wg}}}{100} \right)^3 \right] \quad (3.8)$$

3.2 SOLUTION METHOD

Solution method used in this study is given in a schematic view in Figure 3.3.

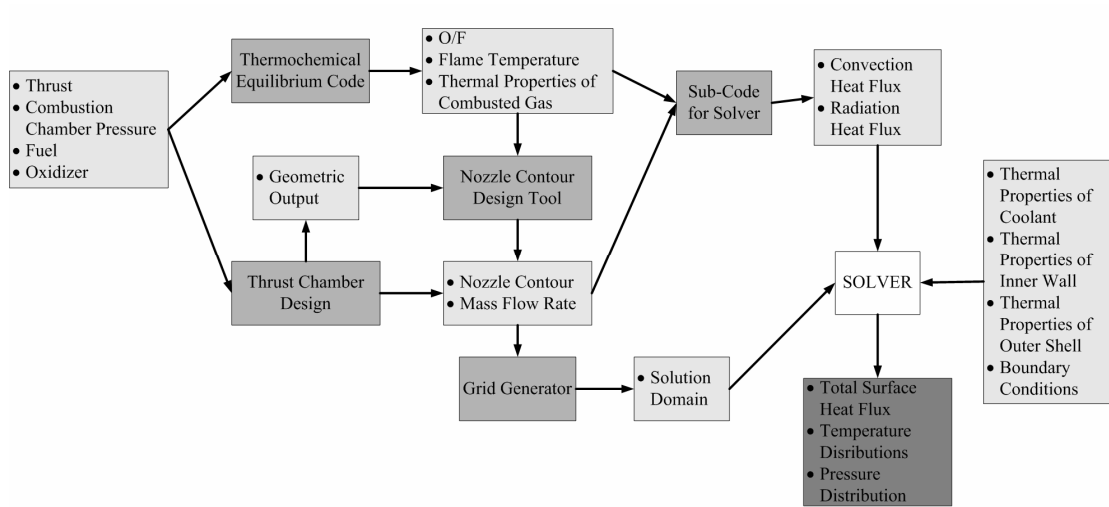


Figure 3.3 – Schematic View of Solution Method

3.2.1 Thermochemical Equilibrium Code

To get thermal properties of the combusted gas, NASA computer program CEA (Chemical Equilibrium with Applications) [7] is used. The program calculates chemical equilibrium product concentrations from any set of reactants and determines thermodynamic and transport properties for the product mixture. Associated with the program are independent databases with transport and thermodynamic properties of individual species.

3.2.2 User Defined Function for Solver

User Defined Function, which is coupled with the solver, basically calculates the heat flux from combusted gases to solution domain in terms of T_{wg} (gas side wall temperature) by using the equations 3.2 and 3.6. Thermal properties of combusted gases are given as an input data from CEA code. The code gets the coordinates of the nodes from the solver to calculate Mach number and area which are used in equation 3.3. Mach numbers are calculated using isentropic gas equations.

3.2.3 Grid Generator and Solver

GAMBIT [13] is used for grid generation. The grid is generated by hexahedral elements in consideration of structured mesh. FLUENT [14], a pressure based segregated solver, is used for the solution. Standard k- ϵ two-equation turbulence model is employed with standard wall functions. SIMPLE algorithm is used to get the pressure field.

CHAPTER 4

VALIDATION

Validation of the solution method was performed using the experimental and numerical studies of Wadel and Meyer [16, 17]. They used 89 kN GH₂ and LOX engine for their experimental studies [17]. The engine specifications are given in Table 4.1.

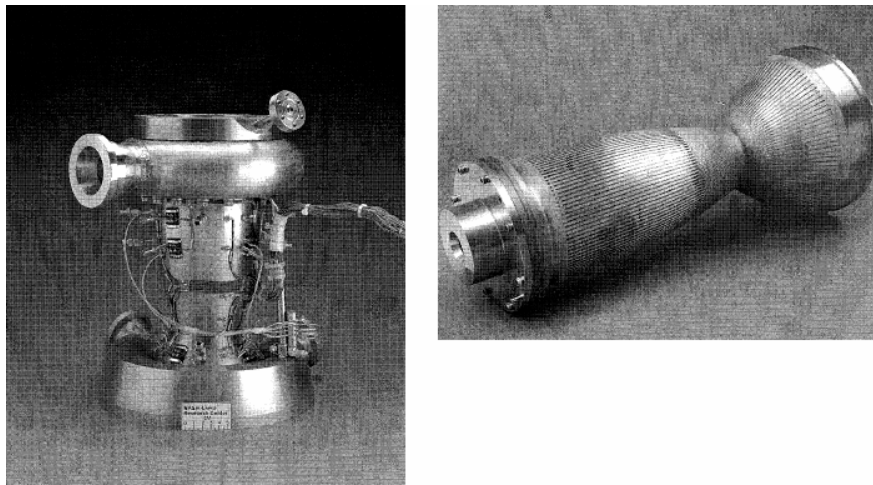


Figure 4.1 – 89 kN GH₂ and LOX Engine [17]

The thrust chamber consisted of an oxygen free high conductivity (OFHC) copper inner wall with a nickel outer shell. The injector had 91 liquid oxygen posts. Chamber liner was milled with 100 conventional coolant channels. These channels had an aspect ratio of 2.5. In the critical heat flux area (nozzle throat region)

cooling channels are bifurcated into 200 channels and aspect ratio was increased up to 8. For bifurcated channel cooling systems, channels were split into two channels and combined back to a single channel.

Table 4.1 – 89 kN GH₂ and LOX Engine Specifications

Thrust [kN]	89
Chamber Pressure [bar]	110
Oxidizer/Fuel	Liquid Oxygen/Gas Hydrogen
O/F	6
Coolant	Liquid Hydrogen
LOX mass flow rate [kg/s]	13.8
GH ₂ mass flow rate [kg/s]	2.3
LH ₂ mass flow rate [kg/s]	2.3
Initial Temperature of LOX [K]	91.7
Initial Temperature of GH ₂ [K]	300
Initial Temperature of LH ₂ [K]	44.4

To get the temperature values on the hot-gas-side wall temperature, nine thermocouples were inserted into holes drilled in the centre of the coolant channel ribs. Also pressure taps were placed in the locations of coolant channel inlet and coolant channel outlet. The tests are performed for different mass flow rates in cooling channels. Gas side wall temperature distributions and pressure drops in the channels are obtained [17].

Their numerical solution method is validated with the experiments explained above. For numerical analysis Rocket Thermal Evaluation code (RTE) and Two-Dimensional Kinetics nozzle performance code (TDK) are used (explained in Chapter 2). Radiation effects are not considered in analysis.

After the validation of their code, Wadel performed a numerical study for comparison of high aspect ratio cooling channel designs [16]. In this study seven different cooling channel designs are compared according to their cooling

efficiencies with considering fabrication. First design is called as “Baseline” and has 100 continuous cooling channels with an aspect ratio of 2.5 and constant cross-sectional area. Fifth design is the bifurcated model which corresponds to the experimental data performed by Wadel and Meyer [17]. For the validation of solution method used in this study these two models are considered.

4.1 Baseline Solution

4.1.1 Grid Generation

Solution domain is generated for 5 cases. For each cases solution domain consist of 3 sub-domains; inner wall, outer shell and coolant. For solid domains tetrahedral elements and for coolant domain hexahedral elements are used. Between the sub-domains non-conformal grid boundary is used. The specifications of the grid for 5 cases are given in Table 4.2 and the cross-section of the solution domains are given in Figure 4.2.

Table 4.2 – Grid Specifications

	CASE 01	CASE 02	CASE 03	CASE 04	CASE 05
Grid Type (Inner Wall)	Tetrahedral	Tetrahedral	Tetrahedral	Tetrahedral	Tetrahedral
# of Elements (Inner Wall)	56,672	56,672	56,672	56,672	56,672
Grid Type (Outer Shell)	Tetrahedral	Tetrahedral	Tetrahedral	Tetrahedral	Tetrahedral
# of Elements (Outer Shell)	104,026	104,026	104,026	104,026	104,026
Grid Type (Coolant)	Hexahedral	Hexahedral	Hexahedral	Hexahedral	Hexahedral
# of Elements (Coolant)	82,134	167,112	450,400	1,014,000	4,563,000
Thickness of First Row (Coolant)	10 μm	5 μm	1 μm	0.5 μm	0.1 μm
Total Number of Elements	211,832	296,810	580,098	1,143,698	4,692,698

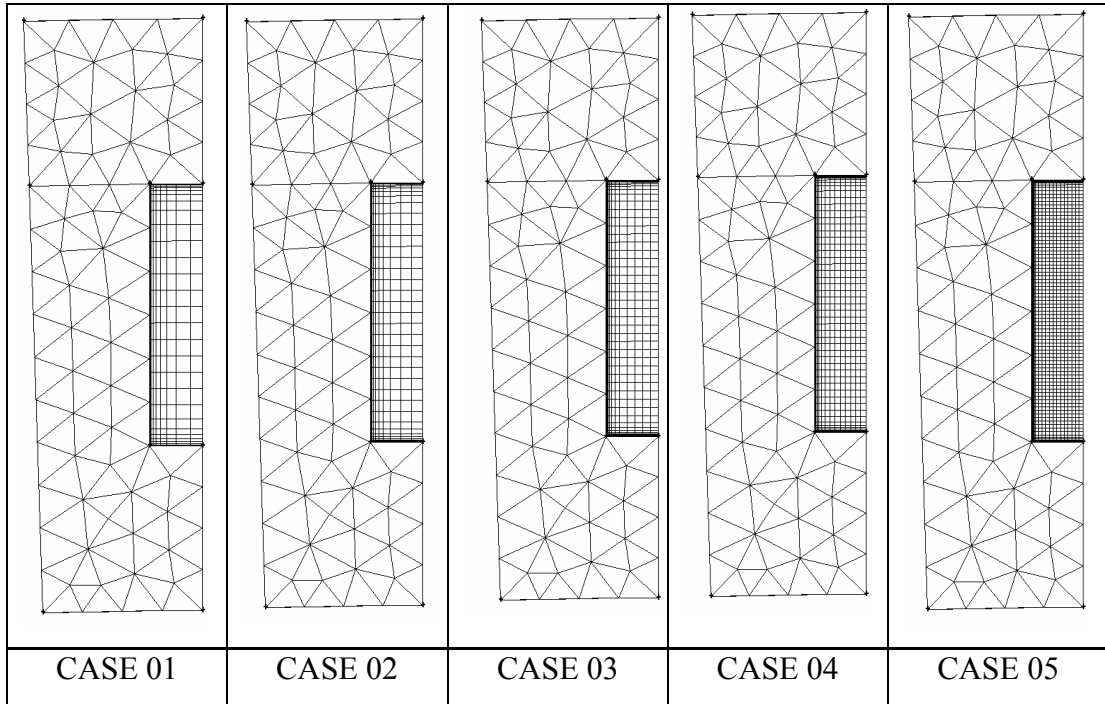


Figure 4.2 – Cross-Sectional View of Solution Domains

4.1.2 Material Properties

Materials used in the analysis are defined as Liquid Hydrogen for the coolant, Oxygen Free High Conductivity Copper for the inner wall and INCONEL-718 for the outer shell. Thermal properties of the materials are given in (Appendix APPENDIX A). Surface roughness for metal structures is taken 3.5 μm by considering milling process [35].

4.1.3 Results and Discussion

Results are obtained for 5 different solution domains. Convergence history of temperature rise and pressure drop in cooling channels according to number of elements, are given in Figure 4.3 and Figure 4.4. Solution results of the five cases along with the Wadel's Solution [16] are given in Table 4.3 and Figure 4.5.

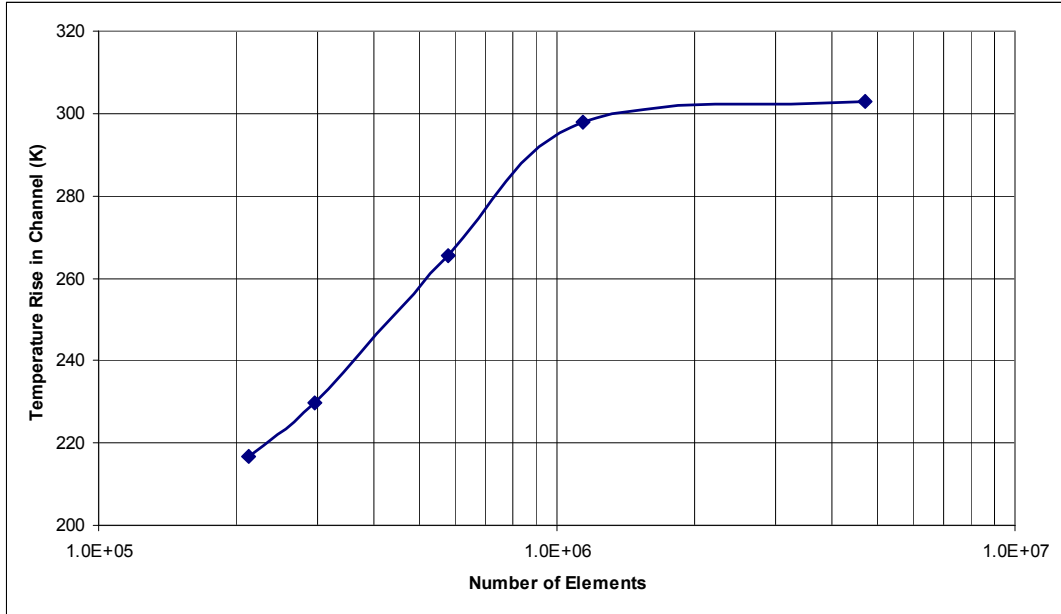


Figure 4.3 – Convergence History of Temperature Rise

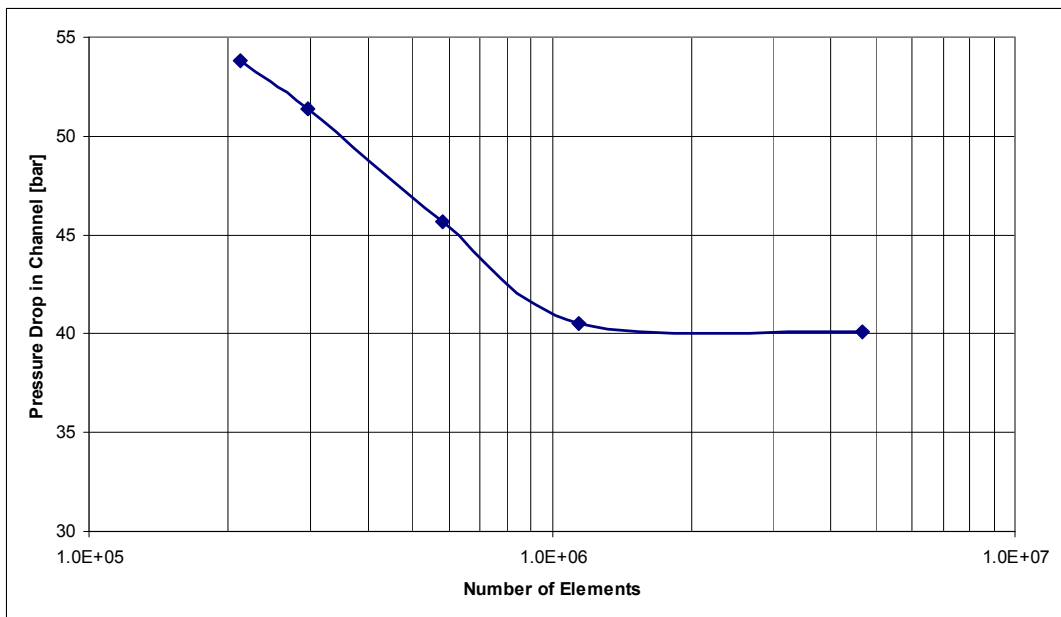


Figure 4.4 – Convergence History of Pressure Drop

Table 4.3 – Results of Baseline Solution

	Tmax on Gas Side Wall [K]	Pressure Drop in Channel ΔP [bar]	Temperature Rise in Channel ΔT [K]
CASE 01	882.7	53.8	216.8
CASE 02	816.9	51.4	229.8
CASE 03	783.2	45.7	265.4
CASE 04	755.07	40.5	297.8
CASE 05	748.4	40.1	302.8
Wadel's Solution	764	37	-

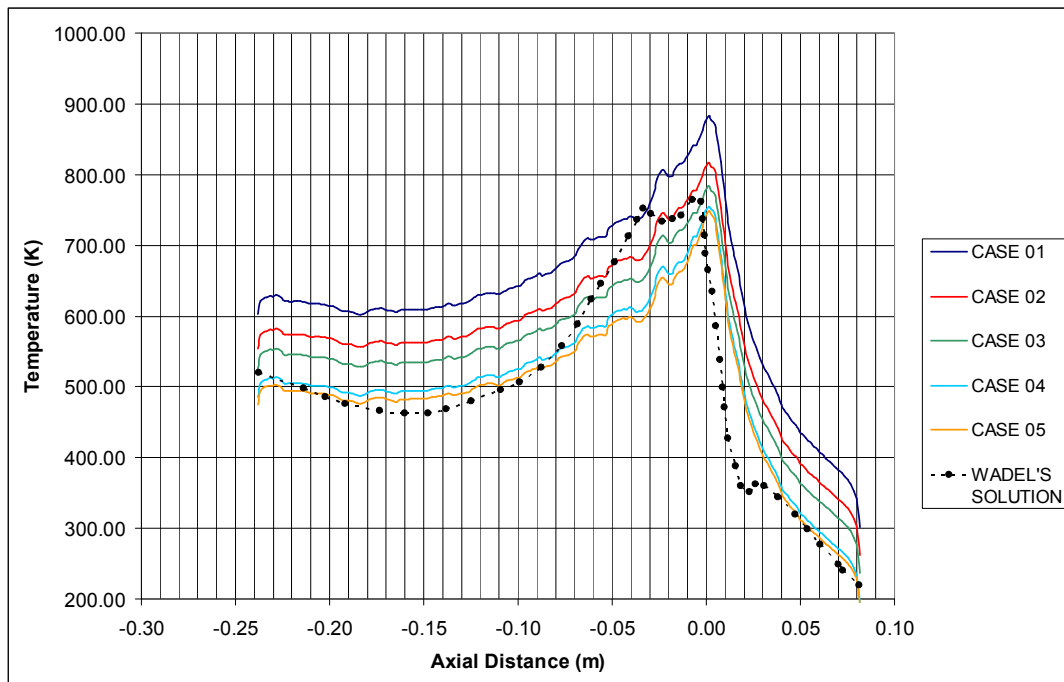


Figure 4.5 – Temperature Distribution on Gas Side Wall for Baseline Solution

As can be seen from the results, as the number of elements increased and the thickness of boundary layer is decreased, the solution is converged. The results for CASE 04 and CASE 05 are quite similar and at this point the grid specifications for CASE 04 are enough to get grid independent solutions. Therefore for the following analysis in this study, grids will be generated according to the grid specifications of CASE 04.

4.2 Bifurcation Channel Solution

By using the grid specifications of CASE 04, the solution domain is generated for bifurcation channel. Results are obtained by present solution method and compared with the numerical and experimental solutions of Wadel and Meyer in Table 4.4 and Figure 4.5

Table 4.4 – Comparison of Pressure Values

	P_{inlet} [bar]	P_{outlet} [bar]	ΔP [bar]
Present Numerical Solution	175.0	138.3	36.7
Wadel's Numerical Solution	175.0	135.5	40.0
Wadel's & Mayer's Experimental Data	175.0	125.0	50.0

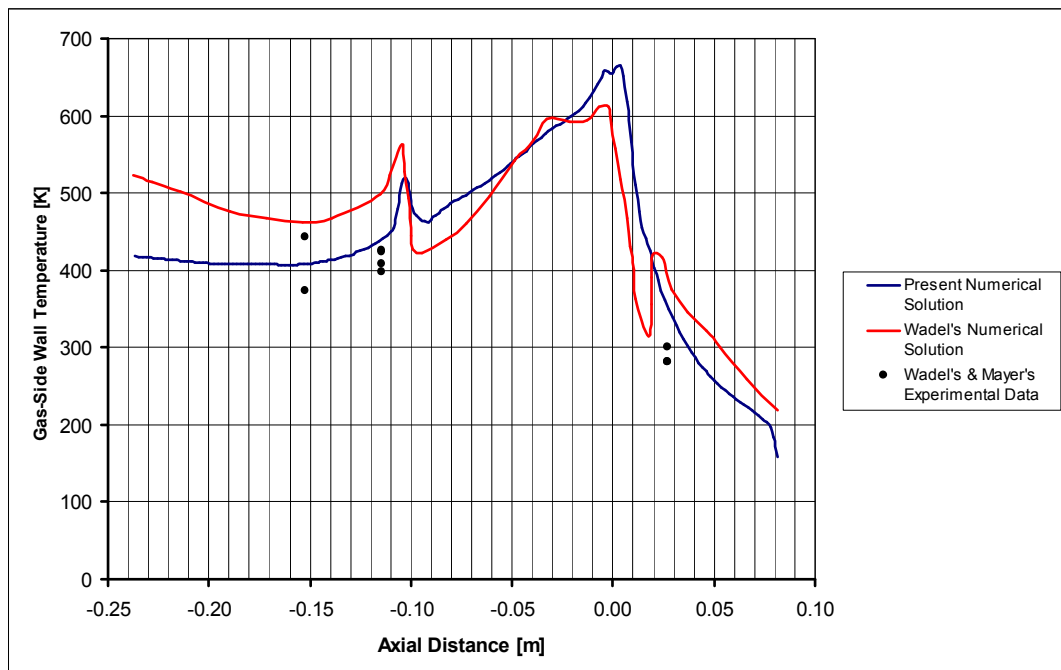


Figure 4.6 – Temperature Distribution on Gas-Side Wall for Bifurcation Channel Solution

4.3 Discussion

For both analysis solutions, the results are quite similar with the numerical and experimental results found in literature. Although there are some minor differences between temperature and pressure values, these differences are acceptable. The reasons for the differences could be the uncertainties on material thermal properties and cooling channel geometry. The numerical solutions are strictly based on thermal properties and channel geometry and these parameters are given roughly in literature.

In this study main aim is to see the effect of cooling channel parameters on cooling efficiency. Therefore the present solution is suitable and sufficient to understand the effect of cooling parameters on efficiency.

CHAPTER 5

THRUST CHAMBER PRELIMINARY DESIGN

Although the design of thrust chamber consists of many parameters and detail calculations, using basic geometric parameters are adequate to understand the regenerative cooling effect on the system. In this study, a preliminary thrust chamber design is performed to get the thrust chamber contour. In Figure 5.1 the scheme of chamber LPRE is given. Region I is the Combustion Region, Region II is the Subsonic Region and Region III is the Supersonic Region. The combination of Region II and Region III can be called as nozzle and Region I as combustion chamber.

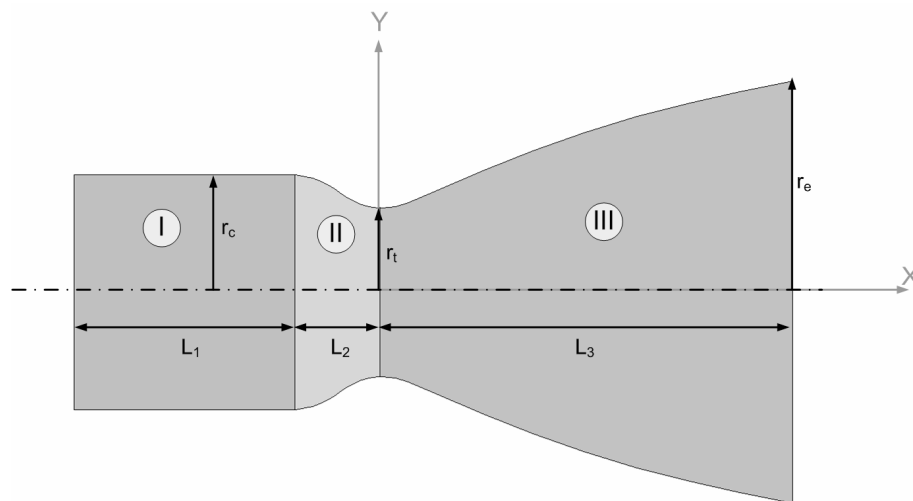


Figure 5.1 – The Scheme of LPRE Chamber

For built-up of gas-dynamic profile of the combustion chamber, it is necessary to give some input data to the system such as thrust (at sea level), chamber pressure, exit pressure, ambient pressure and propellant components. These parameters are given in Table 5.1.

Table 5.1 – LPRE Requirements

Thrust [kN]	300
Combustion Chamber Pressure [bar]	60
Exit Pressure [bar]	1.5
Ambient Pressure [bar]	1
Fuel	Kerosene (RP-1)
Oxidizer	LOX

Oxidizer-fuel ratio is one of the main parameters also. To find the oxidizer-fuel ratio (O/F) for high combustion efficiency, oxidizer-fuel couple with different ratios is combusted by using the thermo-chemical code CEA. For different fuel-oxidizer ratios (O/F), flame temperatures and I_{sp} values are found and given in Table 5.2, obtained graphs are given in Figure 5.2 and Figure 5.3.

Table 5.2 – Flame Temperatures and I_{sp} Values for Different O/F

Mass Percentage of RP-1 [%]	Flame Temperature [K]	I_{sp} [s]
5	1809	164
10	2944	224
15	3402	257
20	3607	278
25	3678	292
30	3570	295
35	3154	281

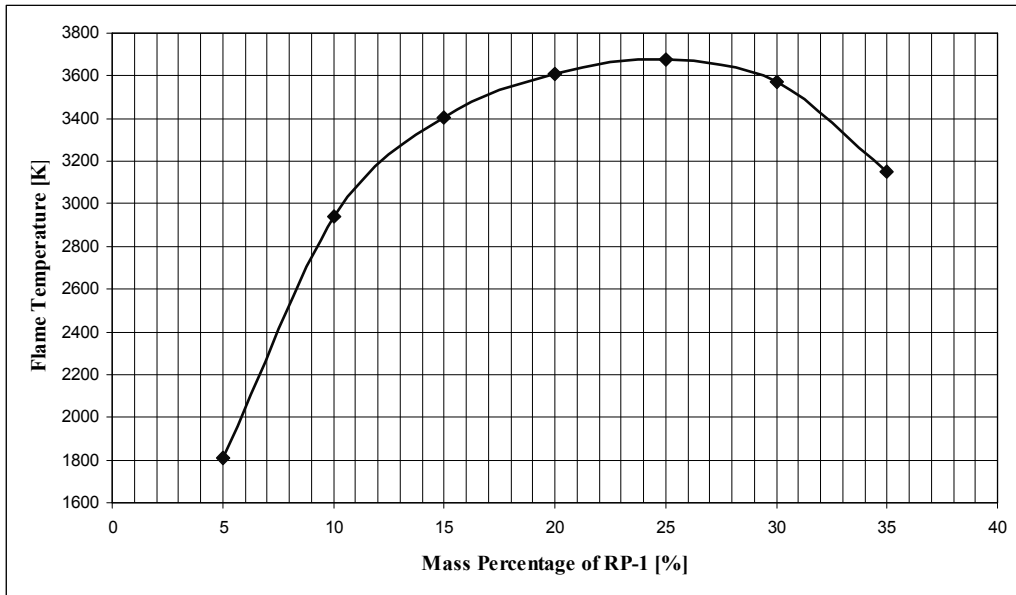


Figure 5.2 – Flame Temperature vs Mass Percentage of RP-1

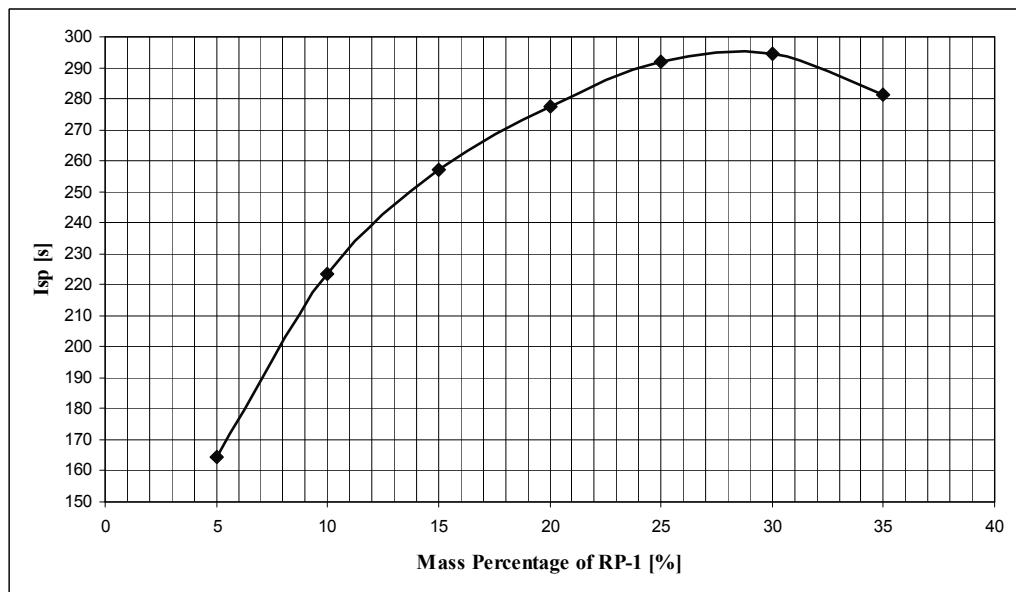


Figure 5.3 – I_{sp} vs Mass Percentage of RP-1

Maximum I_{sp} is obtained around 30 percentage of RP-1. Therefore O/F = 7/3, I_{sp} = 295s and T_f = 3570K are selected for the combustion. Total mass flow rate

and mass flow rates for the propellant and oxidizer can be calculated as given below. For this O/F ratio Specific Heat Ratio (γ) is found as 1.146.

Mass Flow Rate:

$$\dot{m} = \frac{F}{I_{sp}g} \quad (5.1)$$

$$\dot{m} = 103.8 \frac{\text{kg}}{\text{s}}$$

$$\dot{m}_{\text{ox}} = 103.8 \times 0.7 = 72.7 \frac{\text{kg}}{\text{s}}$$

$$\dot{m}_{\text{pr}} = 103.8 \times 0.3 = 31.1 \frac{\text{kg}}{\text{s}}$$

Nozzle Expansion Area Ratio:

$$\varepsilon = \frac{1}{\left(\frac{\gamma+1}{2}\right)^{\frac{1}{\gamma-1}} \left(\frac{P_e}{P_c}\right)^{\frac{1}{\gamma}} \sqrt{\frac{\gamma+1}{\gamma-1} \left[1 - \left(\frac{P_e}{P_c}\right)^{\frac{\gamma-1}{\gamma}}\right]}} \quad (5.2)$$

$$\varepsilon = 6.573$$

Thrust Coefficient:

$$C_f = \sqrt{\frac{2\gamma^2}{\gamma-1} \left(\frac{2}{\gamma+1}\right)^{\frac{\gamma+1}{\gamma-1}} \left[1 - \left(\frac{P_e}{P_c}\right)^{\frac{\gamma-1}{\gamma}}\right]} \varepsilon \frac{P_e - P_a}{P_c} \quad (5.3)$$

$$C_f = 1.6$$

Throat Area:

$$A_t = \frac{F}{C_f P_c} \quad (5.4)$$

$$A_t = 31205\text{mm}^2$$

Throat Diameter:

$$d_t = \sqrt{\frac{4A_t}{\pi}} \quad (5.5)$$

$$d_t = 200\text{mm}$$

Exit Area:

$$A_e = A_t \varepsilon \quad (5.6)$$

$$A_e = 205097\text{mm}^2$$

Exit Diameter:

$$d_e = \sqrt{\frac{4A_e}{\pi}} \quad (5.7)$$

$$d_e = 512\text{mm}$$

5.1 Nozzle Contour Estimation for Region II

The total combustion process; from injection of the reactants until completion of conversion of the reactants to hot product gases, requires finite amount of time and volume which can be defined by Characteristic Length (L^*). L^* can be estimated from experimental data and previously successful designs. Typical

Characteristic Lengths for various propellant combinations are given in Table 5.3. For the following calculation L^* is taken as 1.0m (Liquid Oxygen / RP-1).

Table 5.3 – Typical Characteristic Lengths for Various Propellant Combinations

Propellant Combination	Characteristic Length, L^* [m]
Chlorine Trifluoride / Hydrazine-Base Fuel	0.5 – 0.76
Liquid Fluorine / Hydrazine	0.61 – 0.71
Liquid Fluorine / Gas Hydrogen	0.56 – 0.66
Liquid Fluorine / Liquid Hydrogen	0.64 – 0.76
Hydrogen Peroxide / RP-1	1.52 – 1.78
Nitric Acid / Hydrazine-Base Fuel	0.76 – 0.89
Nitrogen Tetroxide / Hydrazine-Base Fuel	0.76 – 0.89
Liquid Oxygen / Ammonia	0.76 – 1.02
Liquid Oxygen / Gas Hydrogen	0.56 – 0.71
Liquid Oxygen / Liquid Hydrogen	0.76 – 1.02
Liquid Oxygen / RP-1	1.02 – 1.27

Conditional Length:

$$L_c = 0.05\sqrt{2r_t} \quad (5.8)$$

$$L_c = 0.424\text{m}$$

Where L_c in meters and r_t in millimeters.

Nozzle Contraction Area Ratio:

$$\varepsilon_c = \frac{L^*}{L_c} \quad (5.9)$$

$$\varepsilon_c = 2.361$$

Chamber Area:

$$A_c = A_t \varepsilon_c \quad (5.10)$$

$$A_c = 73675 \text{mm}^2$$

Chamber Diameter:

$$d_c = \sqrt{\frac{4A_c}{\pi}} \quad (5.11)$$

$$d_c = 306 \text{mm}$$

Contour of Region II can be estimated by a known formula of Vitoshinsky [10]:

$$y = \frac{r_t}{\sqrt{1 - \left[1 - \left(\frac{r_t}{r_c} \right)^2 \right] \left[1 - \left(\frac{x}{\frac{3}{2}r_c} \right)^2 \right]^2 / \left[1 - \frac{1}{3} \left(\frac{x}{\frac{3}{2}r_c} \right)^2 \right]^3}} \quad (5.12)$$

5.2 Length Estimation for Region I

Volume (Region I and Region II)

$$V_{cc} = A_t \times L^* \quad (5.13)$$

$$V_{cc} = 0.031 \times 10^9 \text{mm}^3$$

V_{II} can be obtained by fitting a curve on Region II contour points and taking the integral of the curve, where $V_{II} = 0.013 \times 10^9 \text{mm}^3$.

$$V_I = V_{cc} - V_{II}$$

$$V_1 = 0.018 \times 10^9 \text{ mm}^3$$

$$L_1 = \frac{V_1}{A_c}$$

$$L_1 = 240 \text{ mm}$$

5.3 Nozzle Contour Estimation for Region III

NCDT (Nozzle Contour Design Tool) Code [11] is used to estimate the nozzle contour for Region III. NCDT is a Fortran based program, which is composed of three parts: Ideal nozzle contour design, Rao nozzle contour design and 2-D axisymmetric, irrotational, inviscid flow analyzer. In this study Rao nozzle contour design tool is used.

5.4 Nozzle Contour for the Designed Thrust Chamber

With the analytical equations and obtained data points the nozzle contour is obtained and given in Figure 5.4.

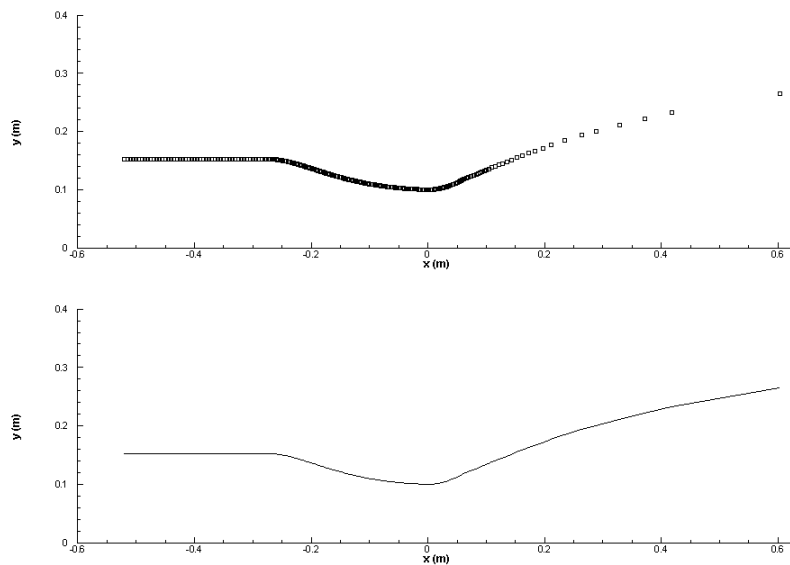


Figure 5.4 – Calculated Combustion Chamber and Nozzle Contour for 300 kN LPRE

CHAPTER 6

ANALYSIS AND RESULTS

Analyses are performed for designed thrust chamber in Chapter 5 for 16 different channel geometries.

6.1 Material Properties

Materials used in the analysis are defined as Kerosene (RP-1) for the coolant, Oxygen Free High Conductivity Copper for the inner wall and INCONEL-718 for the outer shell. Thermal properties of the materials are given in (APPENDIX A). Surface roughness for metal structures is taken $3.5 \mu\text{m}$ by considering milling process [35]

6.2 Boundary Conditions

Boundary conditions for solution domain (Figure 6.1) are given in Table 6.1, Table 6.2 and Table 6.3.

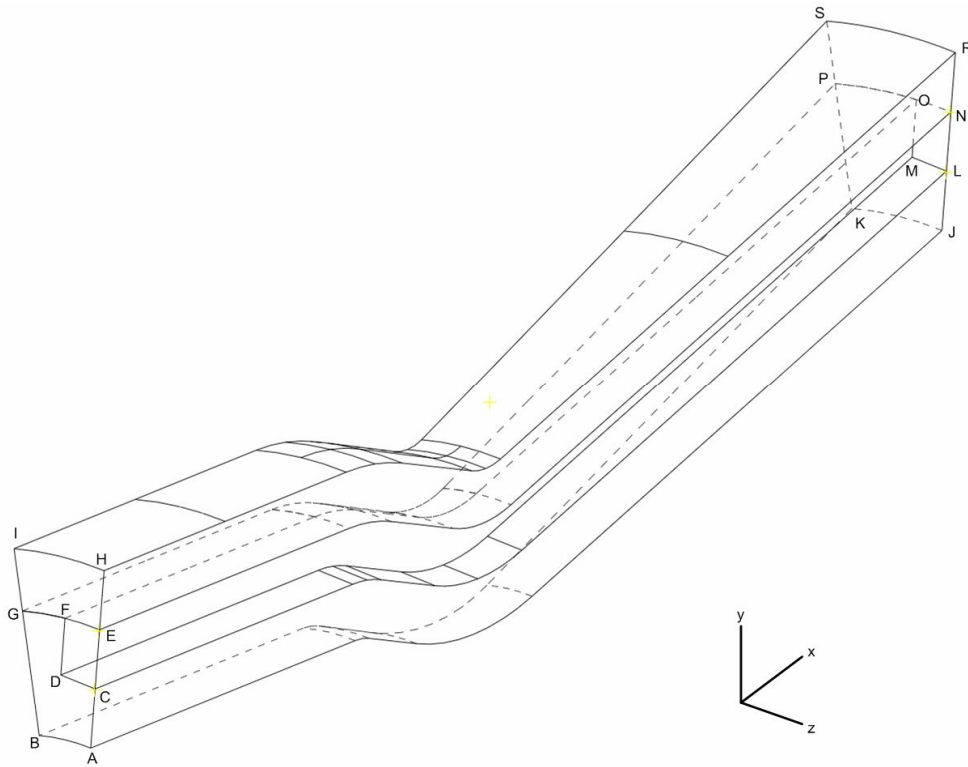


Figure 6.1 – Schematic View of Solution Domain

Table 6.1 – Boundary Conditions for Inner Wall

Plane ABGFDC	$\frac{\partial T}{\partial n} = 0$
Plane JKPOML	$\frac{\partial T}{\partial n} = 0$
Plane BGPk	$\frac{\partial T}{\partial n} = 0$
Plane ACLJ	$\frac{\partial T}{\partial n} = 0$
Plane ABKJ*	$\frac{\partial(kT)}{\partial n} = \dot{q}_g$
(*) Sub-code used for calculating heat flux on plane ABKJ is given in APPENDIX B.	

Table 6.2 – Boundary Conditions for Outer Shell

Plane EFGIH	$\frac{\partial T}{\partial n} = 0$
Plane NOPRS	$\frac{\partial T}{\partial n} = 0$
Plane EHRN	$\frac{\partial T}{\partial n} = 0$
Plane GISP	$\frac{\partial T}{\partial n} = 0$
Plane HIRS	$\frac{\partial T}{\partial n} = 0$

Table 6.3 – Boundary Conditions for Coolant

Plane LMON*	$\dot{m} = \frac{\dot{m}_{pr}}{2 \times N}, T = T_{inlet}$
Plane CDFE**	$P = P_c$
Plane CENL	$\frac{\partial u}{\partial n} = \frac{\partial v}{\partial n} = \frac{\partial w}{\partial n} = \frac{\partial T}{\partial n} = 0$
<p>(*) N refers to number of cooling channels. T_{inlet} is the initial temperature of coolant and 300 K for all analyses.</p> <p>(**) Pressure losses in injector are neglected. Therefore coolant exit pressure should be at combustion chamber pressure in ideal conditions. For all analyses exit pressure of coolant is 60 bar.</p>	

6.3 Effect of Radiation Heat Transfer on Temperature and Pressure

To examine the radiation heat transfer effect, 2 analyses are performed with the same geometry under different heat flux boundary conditions. Analysis parameters are given in Table 6.4.

Table 6.4 – Parameters for Radiation Heat Transfer Investigation

	4x4x100 (no rad)	4x4x100
Channel Height [mm]	4	4
Channel Width [mm]	4	4
# of cooling Channels	100	100
Heat Flux (\dot{q}_g)	Convection	Convection, Radiation
\dot{m} (per channel) [kg/s]	0.311	0.311

Analysis results are given in Table 6.5. Radiation heat transfer increased the total heat flux on thrust chamber wall approximately 1.1 MW/m^2 (8.4 %) at chamber region, 1.2 MW/m^2 (4.4 %) at throat region and 0.7 MW/m^2 (13.1 %) at nozzle exit region (Figure 6.2).

As the total heat flux increased, temperatures on gas side wall and in coolant are increased also. At throat region gas side wall temperature is increased approximately 18 K (2.3 %) and at combustion region coolant temperature is increased approximately 23 K (3.5 %). Temperature distributions for gas side wall and coolant along axial direction are given in Figure 6.3 and Figure 6.4.

There is an inverse proportion between viscosity and temperature for coolant kerosene (Figure A.3). Addition of radiation heat transfer increased the overall temperature of coolant and result in slightly less pressure drop in cooling channel (Figure 6.5).

As a result radiation heat transfer should be considered for regeneratively cooled thrust chambers with hydrocarbon fuels. Therefore for the following analyses sum of radiation heat flux and convection heat flux is used as a boundary condition for gas side thrust chamber wall.

Table 6.5 – Results for Radiation Heat Transfer Investigation

	4x4x100 (no rad)	4x4x100
Maximum Heat Flux on Gas Side Wall [MW/m ²]	28.43	29.32
Maximum Wall Temperature on Gas Side Wall [K]	783.7	801.8
Maximum Coolant Temperature [K]	647.1	669.8
Required Pressure Inlet for Coolant [bar]	78.1	77.8
Pressure Drop in Channel [bar]	18.1	17.8

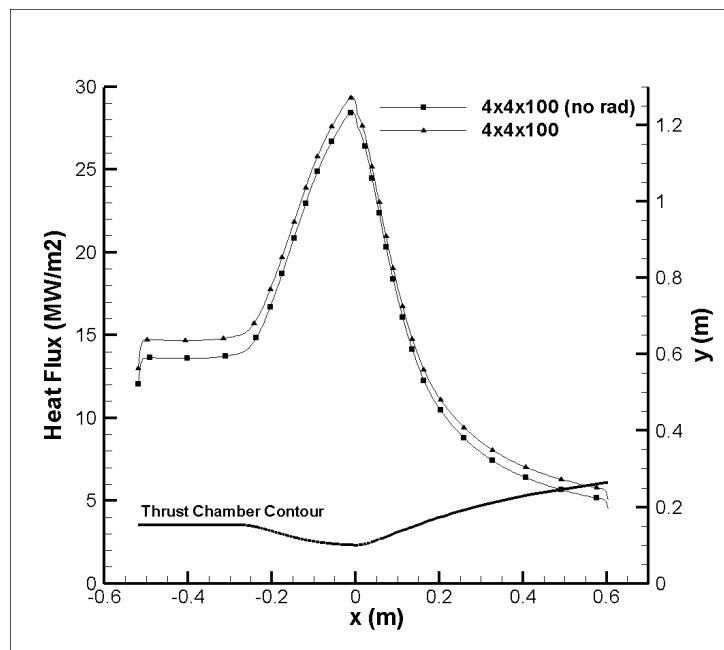


Figure 6.2 – Heat Flux Distribution on Gas Side Wall along Axial Direction for Radiation Heat Transfer Investigation

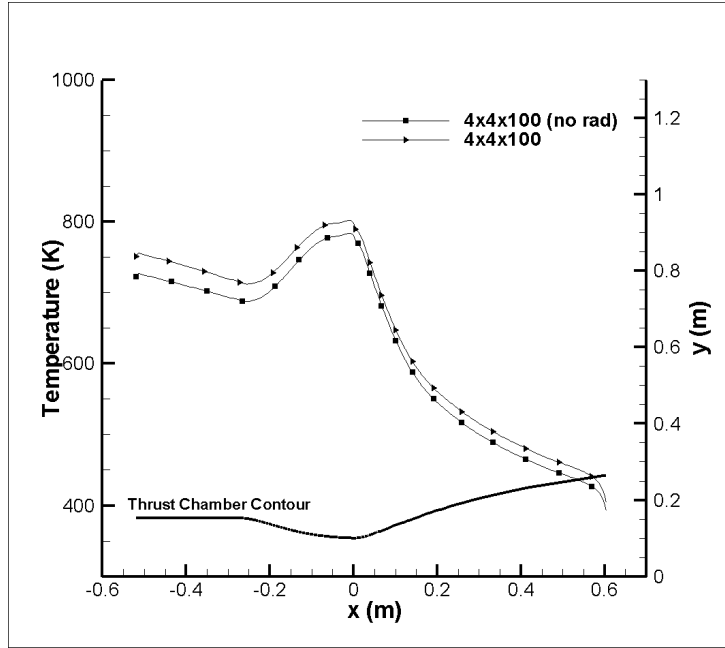


Figure 6.3 – Temperature Distribution on Gas Side Wall along Axial Direction for Radiation Heat Transfer Investigation

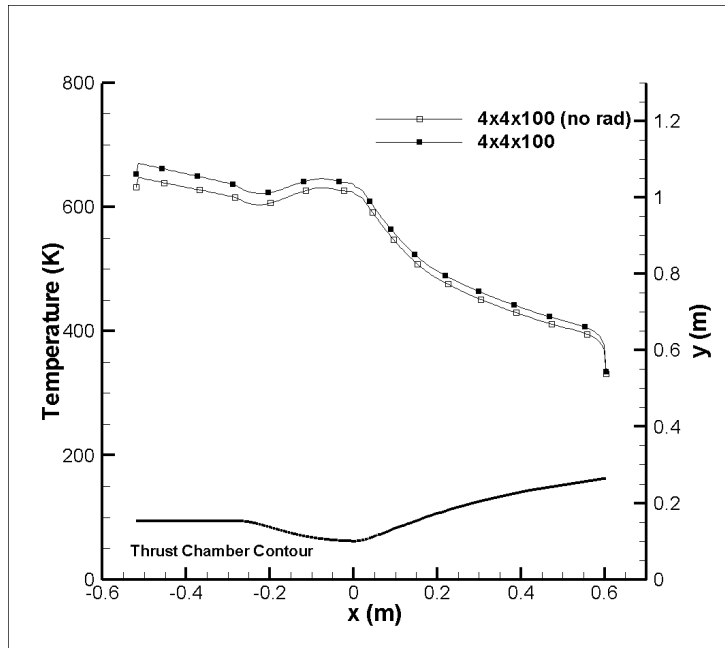


Figure 6.4 – Temperature Distribution of Coolant on Coolant Side Wall along Axial Direction for Radiation Heat Transfer Investigation

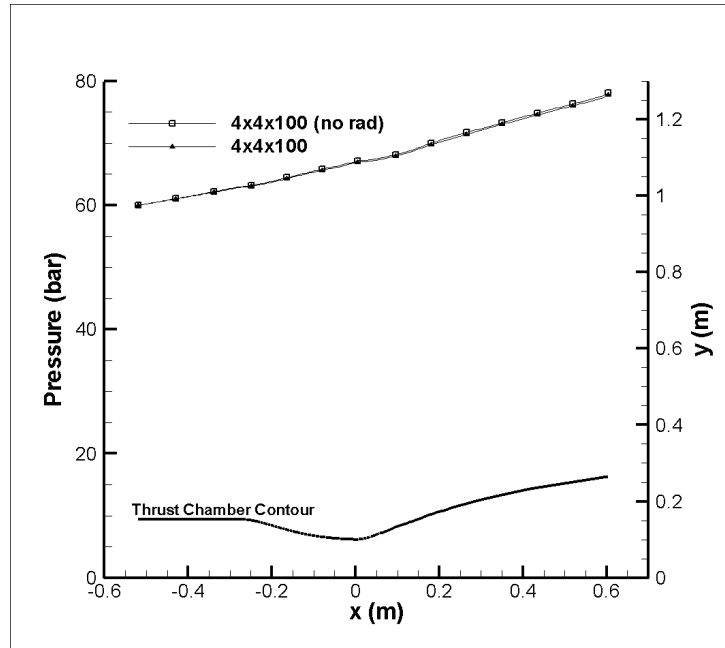


Figure 6.5 – Pressure Distribution of Coolant along Axial Direction for Radiation Heat Transfer Investigation

6.4 Effect of Channel Geometry on Cooling Efficiency

The effect of channel geometry on cooling efficiency will be examined in two groups. In each group the height of the cooling channels are constant and width of the channels are decreased gradually. For the first group height is 4 mm and for the second group height is 8 mm. Analysis parameters are given in Table 6.6 and Table 6.7.

Table 6.6 – Parameters for 4 mm Height Channels

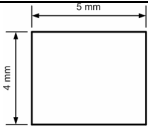
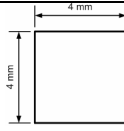
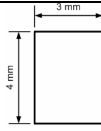
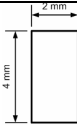
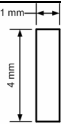
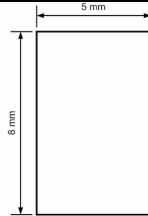
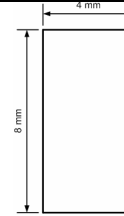
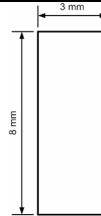


	4x5x100	4x4x100	4x3x100	4x2x100	4x1x100
Channel Height [mm]	4	4	4	4	4
Channel Width [mm]	5	4	3	2	1
# of cooling Channels	100	100	100	100	100
AR (Aspect Ratio)	0.8	1.0	1.3	2.0	4
D_h [mm]	4.4	4.0	3.4	2.7	1.6
Heat Flux (\dot{q}_g)	Convection Radiation	Convection Radiation	Convection Radiation	Convection Radiation	Convection Radiation
\dot{m} (per channel) [kg/s]	0.311	0.311	0.311	0.311	0.311
Channel Geometry					

Table 6.7 – Parameters for 8 mm Height Channels

	8x5x100	8x4x100	8x3x100	8x2x100	8x1x100
Channel Height [mm]	8	8	8	8	8
Channel Width [mm]	5	4	3	2	1
# of cooling Channels	100	100	100	100	100
AR (Aspect Ratio)	1.6	2.0	2.7	4.0	8.0
D_h [mm]	6.2	5.3	4.4	3.2	1.8
Heat Flux (\dot{q}_g)	Convection Radiation	Convection Radiation	Convection Radiation	Convection Radiation	Convection Radiation
\dot{m} (per channel) [kg/s]	0.1555	0.1555	0.1555	0.1555	0.1555
Channel Geometry					

The results are given in Table 6.8 and Table 6.9.

Table 6.8 – Results for 4 mm Height Channels

	4x5x100	4x4x100	4x3x100	4x2x100	4x1x100
Maximum Heat Flux on Gas Side Wall [MW/m ²]	29.03	29.32	29.53	29.67	29.74
Maximum Wall Temperature on Gas Side Wall [K]	822.3	801.8	787.5	777.9	773.2
Maximum Coolant Temperature [K]	681.2	669.8	659.2	649.7	640.3
Required Pressure Inlet for Coolant [bar]	70.3	77.8	96.3	164.0	741.0
Pressure Drop in Channel [bar]	10.3	17.8	26.3	104.0	681.0

Table 6.9 – Results for 8 mm Height Channels

	8x5x100	8x4x100	8x3x100	8x2x100	8x1x100
Maximum Heat Flux on Gas Side Wall [MW/m ²]	27.33	27.90	28.36	28.79	29.24
Maximum Wall Temperature on Gas Side Wall [K]	944.5	904.9	872.5	842.7	811.8
Maximum Coolant Temperature [K]	805.0	760.6	724.0	703.4	679.0
Required Pressure Inlet for Coolant [bar]	61.9	63.4	67.6	83.3	247.2
Pressure Drop in Channel [bar]	1.9	3.4	7.6	23.3	187.2

As given in Chapter 2, heat transfer coefficient is highly depends on Re number ($Re^{0.8}$) and Re number is described as:

$$Re = \frac{\rho u D_h}{\mu} \quad (6.1)$$

For incompressible flows:

$$u = \frac{\dot{m}}{\rho A} = \frac{\dot{m}}{\rho h w} \quad (6.2)$$

$$D_h = \frac{4hw}{2(h+w)} \quad (6.3)$$

$$Re = \frac{\rho}{\mu} \frac{\dot{m}}{\rho hw} \frac{4hw}{2(h+w)} = \frac{2}{\mu} \dot{m} \frac{1}{(h+w)} \quad (6.4)$$

As a result, with the same mass flow rate (same number of cooling channels) and channel height, as we decrease the width of the cooling channel (increasing aspect ratio), Velocity, Re number and heat transfer coefficient on coolant side wall will increase assuming of constant thermal properties. Velocity profiles of the coolant at throat (x=0) for each geometry are given in Figure 6.6.

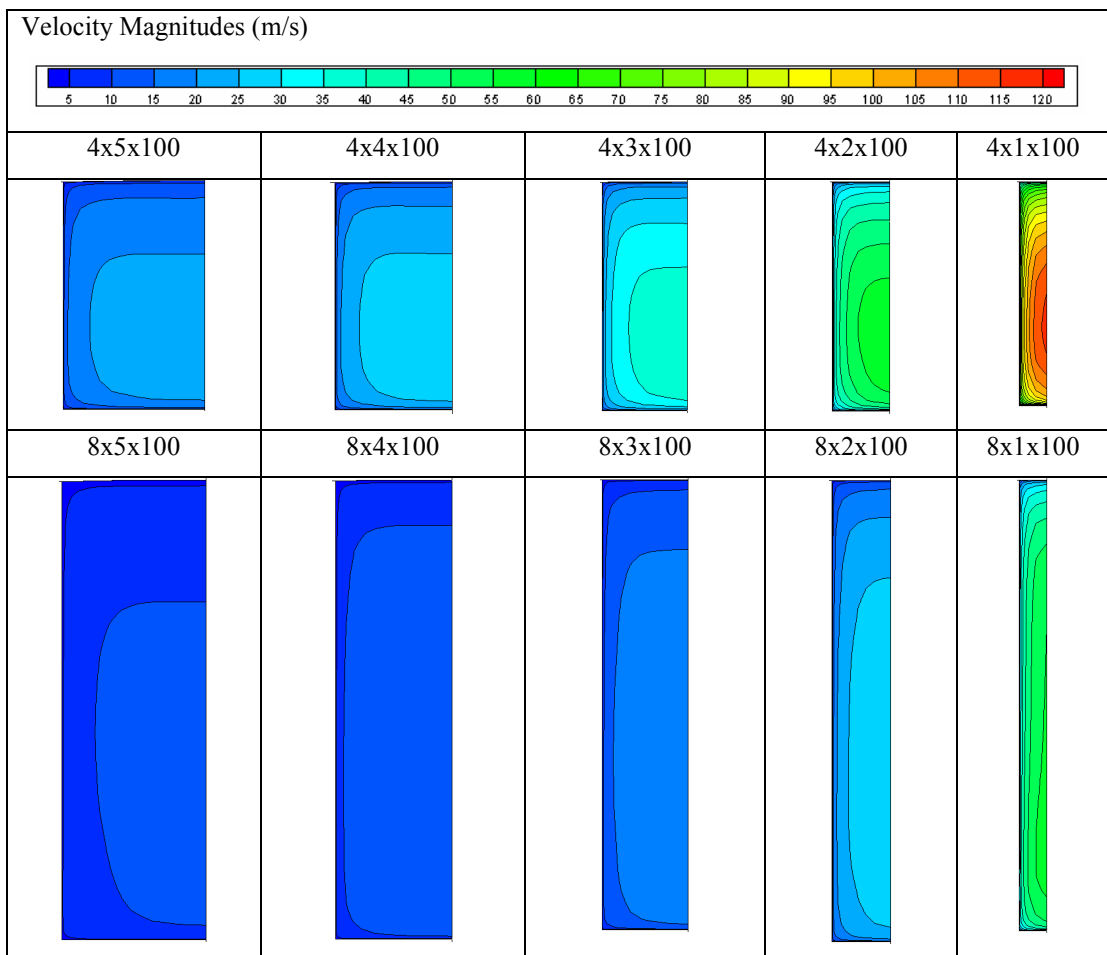


Figure 6.6 – Velocity Profiles of Coolant at Throat (x=0)

Increasing heat transfer coefficient by increasing aspect ratio on coolant side will result in increasing total surface heat flux on gas side wall. In Figure 6.7 and Figure 6.8 total surface heat flux distribution along axial direction is given for 4 mm and 8 mm channel heights. For 4 mm channel heights total surface heat flux is increased 2.5 % between the maximum and minimum aspect ratio cooling channels and for 8 mm cooling channel heat flux is increased 7.0 % at throat section. As the total surface heat flux is increased, temperature difference between gas domain and thrust chamber wall will increase with an assumption of constant heat transfer coefficient and as a result temperature on gas side wall and coolant side wall will decrease as the aspect ratio is increased. Temperature distribution along axial direction on gas side wall and coolant side wall are given in Figure 6.9, Figure 6.10, Figure 6.11 and Figure 6.12 for 4 mm and 8 mm channel heights.

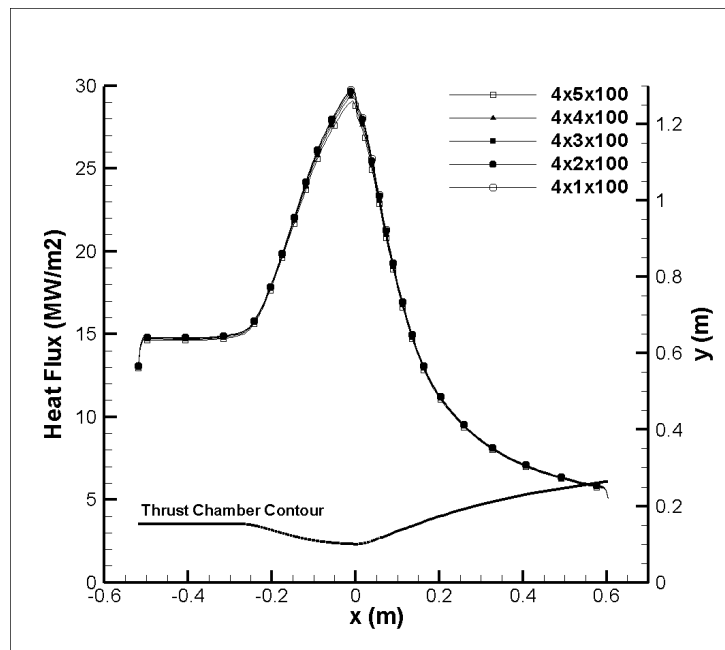


Figure 6.7 – Heat Flux Distribution on Gas Side Wall along Axial Direction for 4 mm Channel Height

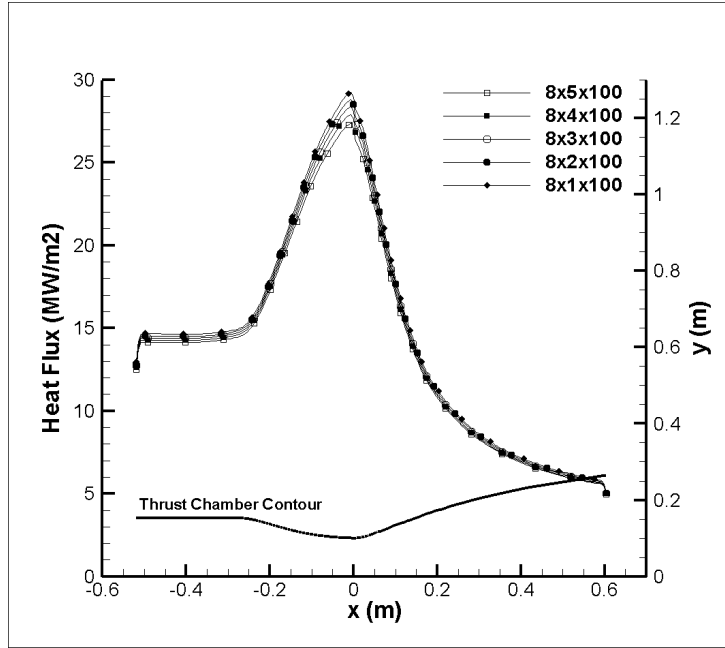


Figure 6.8 – Heat Flux Distribution on Gas Side Wall along Axial Direction for 8 mm Channel Height

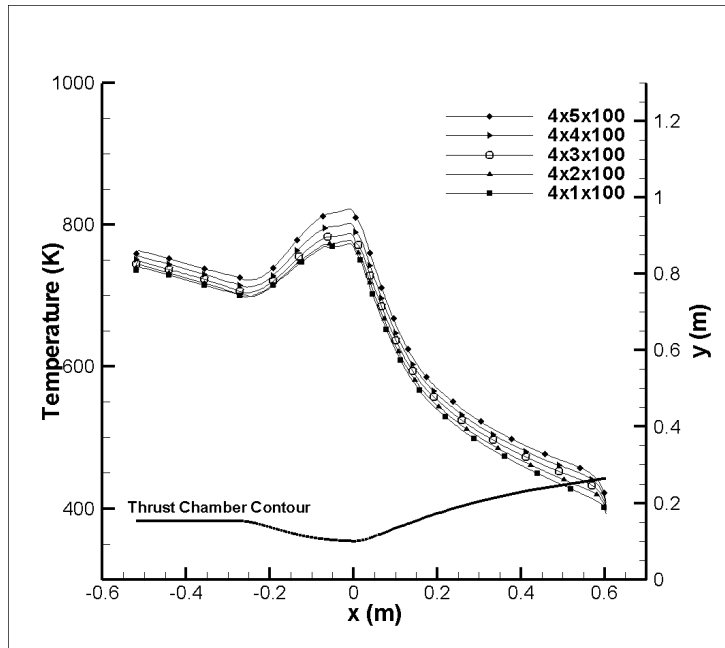


Figure 6.9 – Temperature Distribution on Gas Side Wall along Axial Direction for 4mm Channel Height

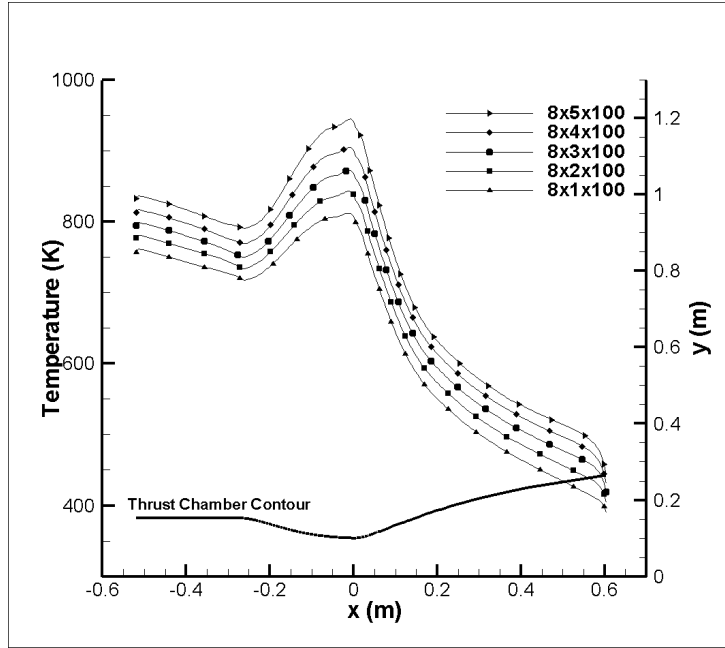


Figure 6.10 – Temperature Distribution on Gas Side Wall along Axial Direction for 8 mm Channel Height

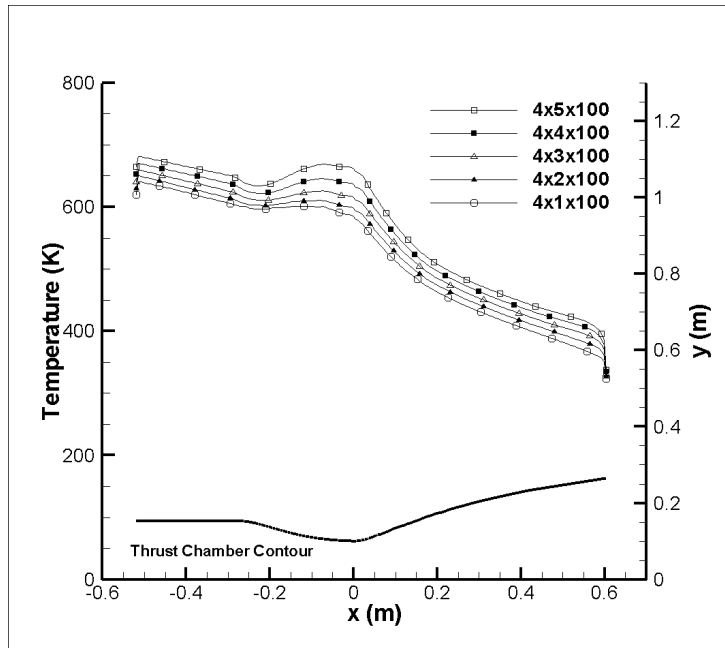


Figure 6.11 – Temperature Distribution of Coolant on Coolant Side Wall along Axial Direction for 4 mm Channel Height

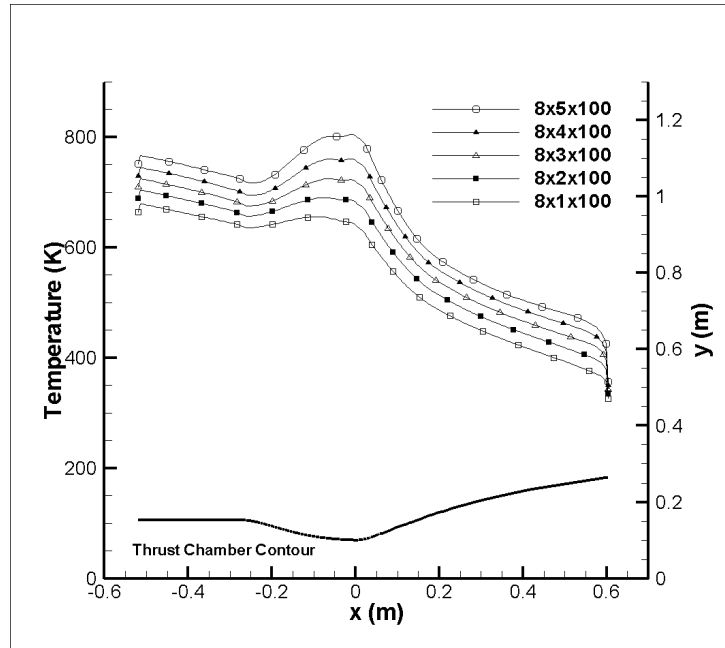


Figure 6.12 – Temperature Distribution of Coolant on Coolant Side Wall along Axial Direction for 8mm Channel Height

With constant channel height and channel number the cooling efficiency is expected to reach an optimum level, because as we increase the aspect ratio, heat transfer area for the coolant decreases and after a while coolant efficiency will start to decrease. As given in Figure 6.13 Figure 6.14, increasing aspect ratio causes a converging solution for minimum temperature on gas side wall and coolant. In this study this optimum level has not been considered as a design point.

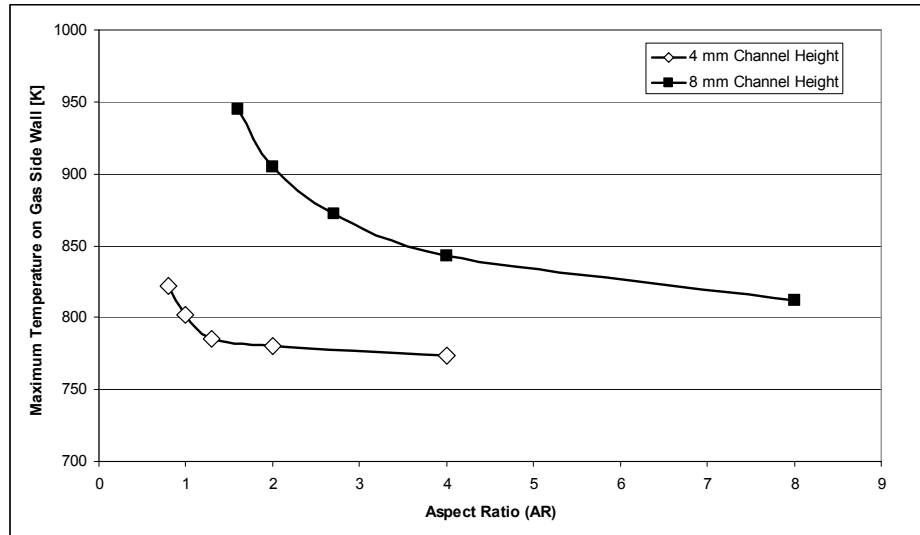


Figure 6.13 – Effects of Aspect Ratio on Gas Side Wall Temperature

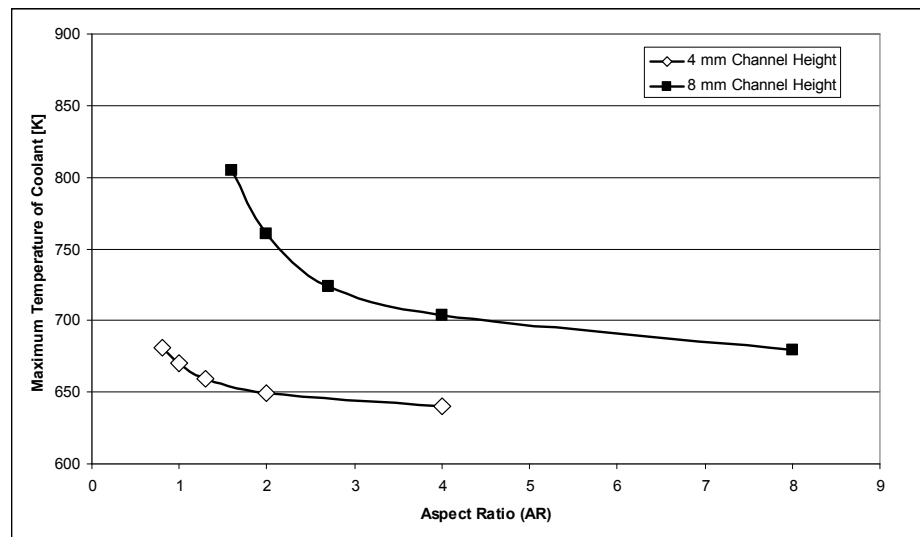


Figure 6.14 – Effects of Aspect Ratio on Coolant Temperature

Pressure drop in coolant channel can be approximated as given in Chapter 2.

$$\Delta P = f \frac{L}{D_h} \frac{\rho V^2}{2} \quad (6.5)$$

$$\Delta P = fL\dot{m}^2 \frac{(w + h)}{4(wh)^2} \quad (6.6)$$

In equation 6.6 with constant channel height and mass flow rate, as we decrease the channel width, pressure of coolant and pressure drop in coolant channel will increase (Figure 6.15 – Figure 6.17). For channel geometries 4x2x100, 4x1x100 and 8x1x100 pressure drops are calculated as higher than the combustion chamber pressure (60 bar) and these designs are not acceptable since they need large feeding systems. Pressure drops around half of the combustion chamber pressure can be used as a system design criteria.

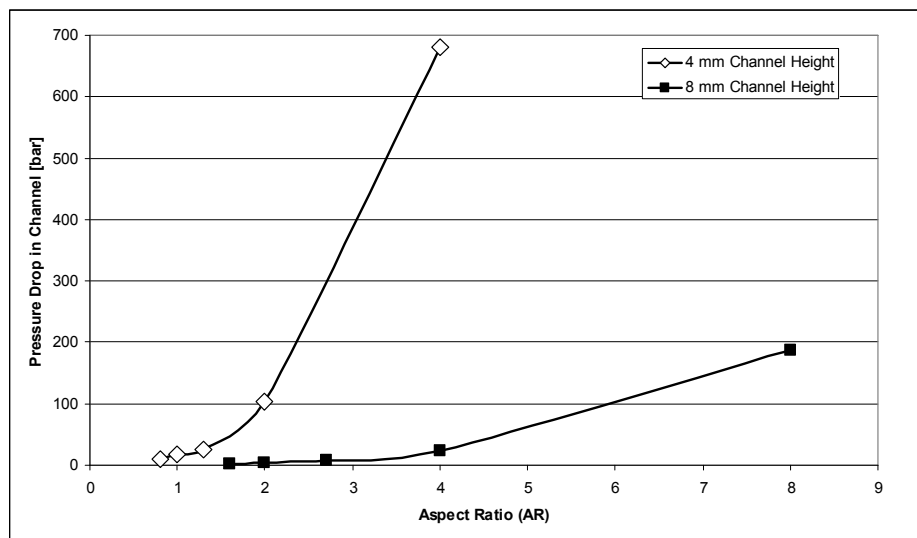


Figure 6.15 – Effects of Aspect Ratio on Pressure Drop in Channel

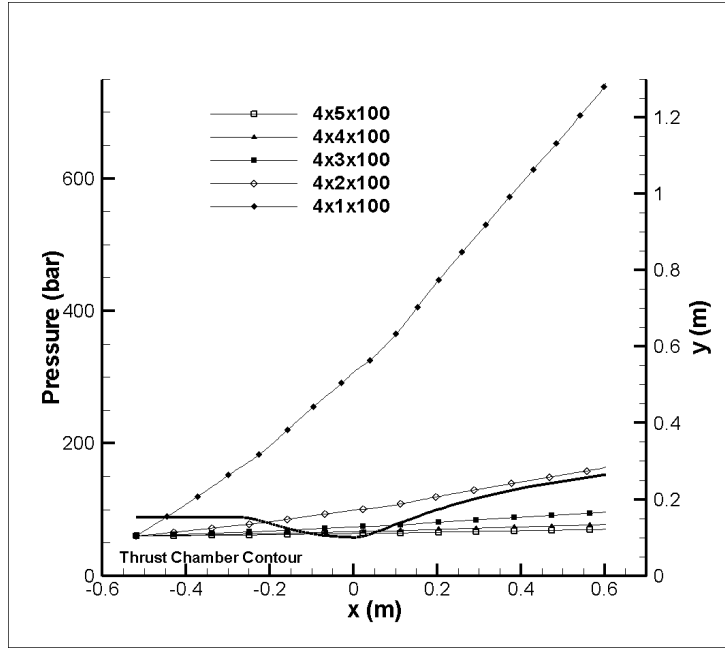


Figure 6.16 – Pressure Distribution of Coolant along Axial Direction for 4 mm Channel Height

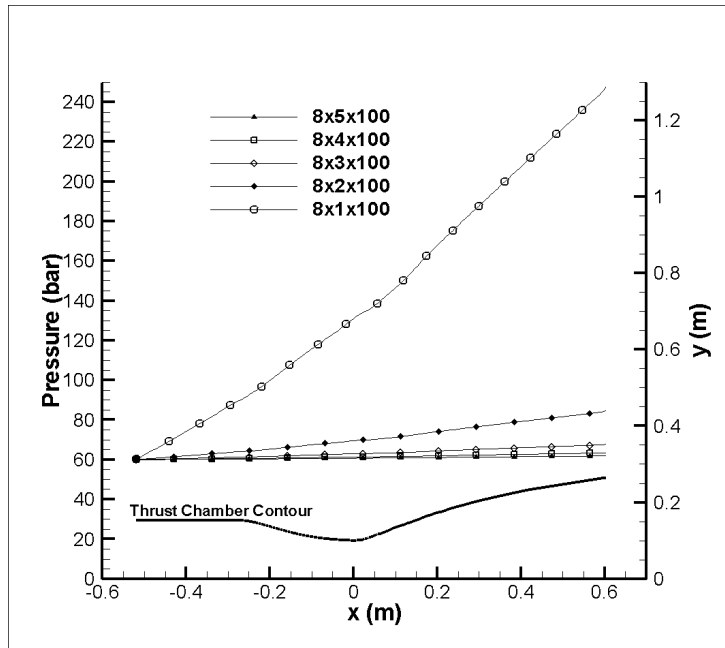


Figure 6.17 – Pressure Distribution of Coolant along Axial Direction for 8 mm Channel Height

6.5 Effect of Number of Channels on Cooling Efficiency

According to the analysis results obtained in section 6.4, coolant channels with $4 \times 1 \text{ mm}^2$ and $4 \times 2 \text{ mm}^2$ cross section area have the best temperature results for cooling but have high pressure drops in the channel. (681 bar and 104 bar respectively). Although it is stated that these two geometries are not suitable because of high pressure drops in coolant channel, by changing the number of coolant channels, it is possible to decrease pressure drop and temperatures on solid body.

Since the cooling efficiency is quite close for these geometries, there is no need to work on case with $4 \times 1 \text{ mm}^2$ which has a very high pressure drop. Therefore, channel geometry with $4 \times 2 \text{ mm}^2$ cross section area is selected to investigate the effect of number of channels on cooling efficiency.

The effect of number of channels on cooling efficiency is investigated for 6 different channel numbers. Analysis parameters are given in Table 6.10.

Table 6.10 – Parameters for Number of Channels Investigation

	4x2x50	4x2x100	4x2x150	4x2x200	4x2x250	4x2x300
Channel Height [mm]	4	4	4	4	4	4
Channel Width [mm]	2	2	2	2	2	2
# of cooling Channels	50	100	150	200	250	300
AR (Aspect Ratio)	2.0	2.0	2.0	2.0	2.0	2.0
D_h [mm]	2.7	2.7	2.7	2.7	2.7	2.7
Heat Flux (\dot{q}_g)	Convection Radiation	Convection Radiation	Convection Radiation	Convection Radiation	Convection Radiation	Convection Radiation
\dot{m} (per channel) [kg/s]	0.6220	0.3110	0.2073	0.1555	0.1244	0.1037

The results are given in Table 6.11. For less number of coolant channels mass flow rate of the coolant is high and for the same cross-section area coolant velocities are high. Velocity profiles of coolant are given at throat region ($x=0$) in Figure 6.18.

Table 6.11 – Results for Channel Number Investigation

	4x2x50	4x2x100	4x2x150	4x2x200	4x2x250	4x2x300
Maximum Heat Flux on Gas Side Wall [MW/m^2]	29.07	29.67	29.83	29.71	29.39	28.67
Maximum Wall Temperature on Gas Side Wall [K]	821.7	777.9	770.5	778.6	800.6	850.1
Maximum Coolant Temperature [K]	654.8	649.7	647.3	649.3	654.4	695.5
Required Pressure Inlet for Coolant [bar]	411.9	164.0	110.8	90.3	80.3	74.6
Pressure Drop in Channel [bar]	351.9	104.0	50.8	30.3	20.3	14.6

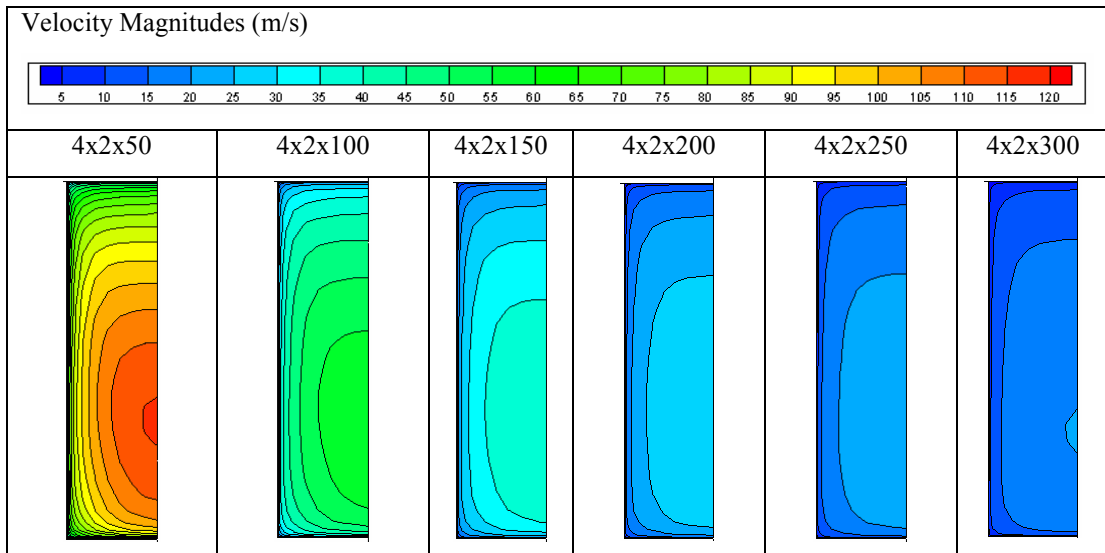


Figure 6.18 – Velocity Profiles of Coolant at Throat ($x=0$)

Maximum coolant side heat transfer coefficient is obtained for geometry with 50 channels but also this geometry has the minimum total heat transfer area between

the coolant and solid body is low. As we increase the number of channels, total heat transfer area is increased. The results show that there exists an optimum number of cooling channels which has the highest heat flux on gas side wall and lowest temperature on gas side wall (Figure 6.19) and coolant (Figure 6.20). For 4x2 mm cross-section area optimum number of cooling channels for cooling efficiency is around 150. Gas side heat flux distribution and temperature distributions for gas side wall and coolant side wall are given in Figure 6.21, Figure 6.22 and Figure 6.23.

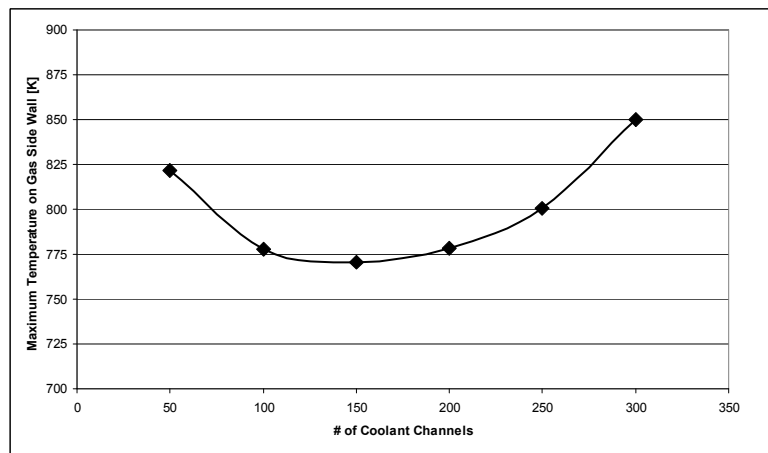


Figure 6.19 – Effects of Number of Channels on Gas Side Wall Temperature

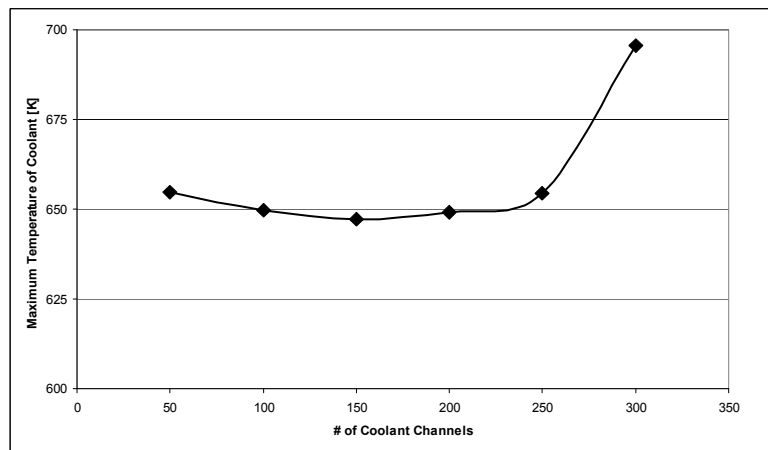


Figure 6.20 – Effects of Number of Channels on Coolant Temperature

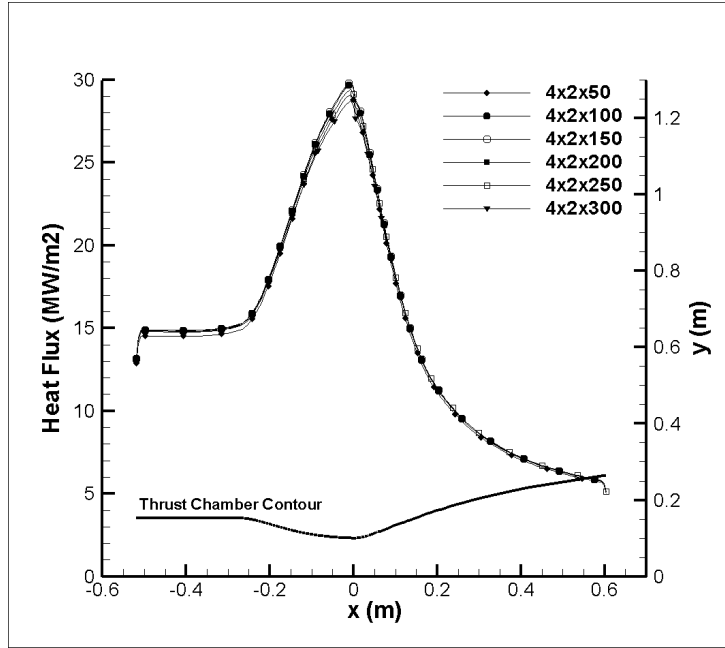


Figure 6.21 – Heat Flux Distribution on Gas Side Wall along Axial Direction for Different Number of Cooling Channels

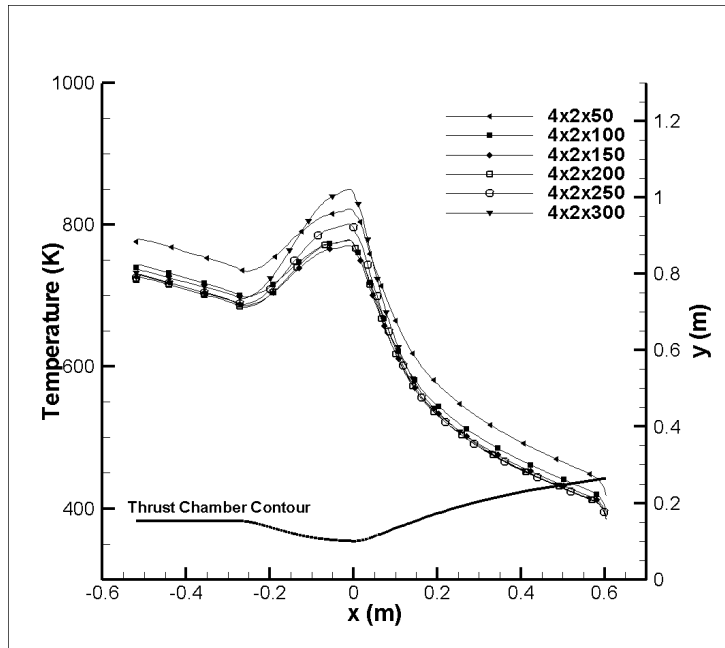


Figure 6.22 – Temperature Distribution on Gas Side Wall along Axial Direction for Different Number of Cooling Channels

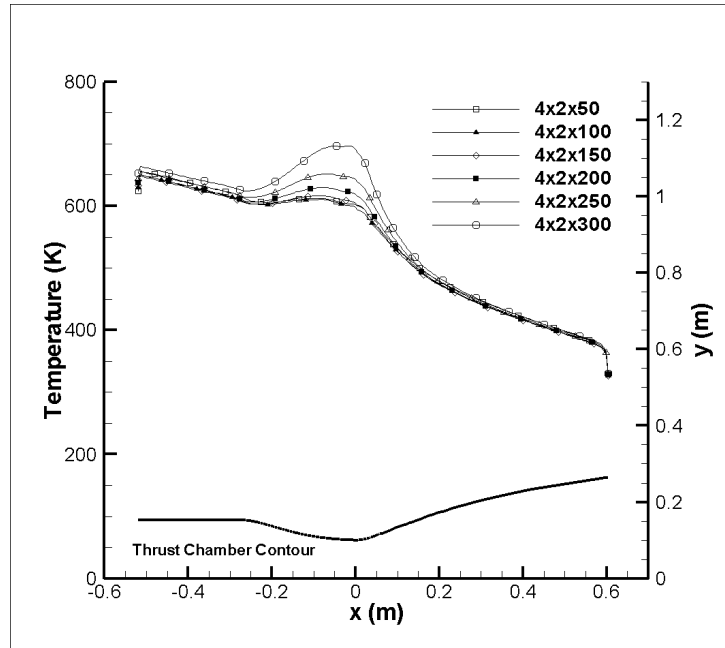


Figure 6.23 – Temperature Distribution of Coolant on Coolant Side Wall along Axial Direction for Different Number of Cooling Channels

Since the velocity magnitudes are decreased as the number of cooling channels are increased, it is obvious to see lower pressure values in coolant channel with high number of coolant channels (Figure 6.24). Pressure distributions along axial direction for different number of coolant channels are given in Figure 6.25

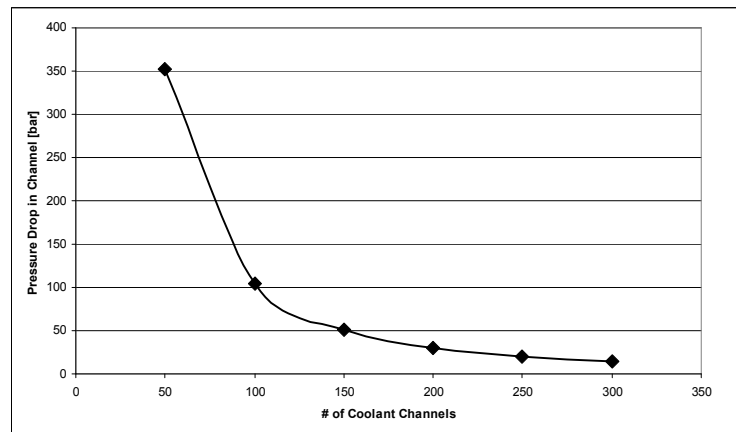


Figure 6.24 – Effects of Number of Channels on Pressure Drop

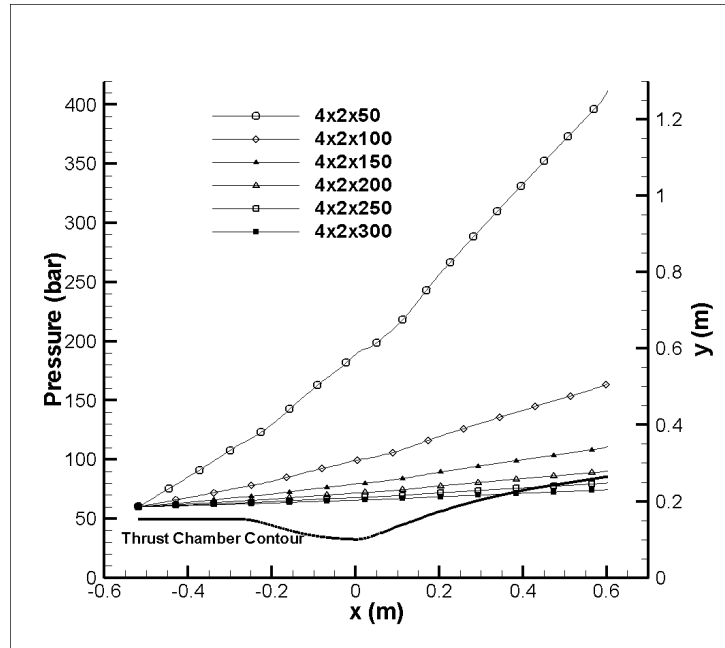


Figure 6.25 – Pressure Distribution of Coolant along Axial Direction for Different Number of Channels

In summary by changing the number of cooling channels maximum gas side wall temperature decreased from 777.9 K to 770.5 K (1.0 %), maximum coolant temperature decreased from 649.7 K to 647.3 K (0.4 %) and pressure drop decreased from 104.0 bar to 50.8 bar (51.2 %). Although the pressure drop is decreased by changing the number of cooling channels, 50.8 bar pressure drop is still high. By changing the cross section area of cooling channel for non critical regions (low heat flux regions), it is possible to decrease pressure drop. This topic will be discussed in next section.

6.6 Cooling Channels with Variable Cross Section Area

To understand the effects of variable cross section on temperature and pressure, new cooling channel geometry is formed. The channel has $4 \times 2 \text{ mm}^2$ cross section area in the throat region and $4 \times 4 \text{ mm}^2$ cross section areas in the combustion region and nozzle region. The geometry of cooling channel is given in Figure 6.26.

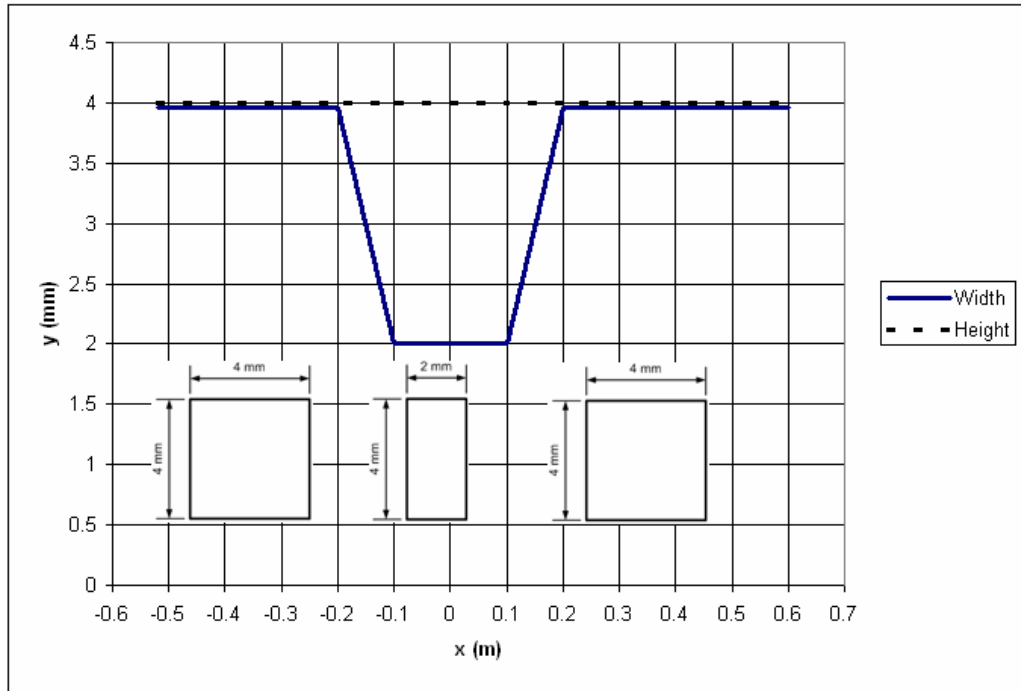


Figure 6.26 – Channel Geometry for Variable Cross Section Area

Results are compared with the 4x2x150 channel geometry and given in Table 6.12. Although there is not a big difference for the maximum heat flux and maximum wall temperature on gas side wall, maximum temperature of coolant is increased approximately 30 K and the pressure drop in the cooling channel decreased to 18.4 bar.

Table 6.12 – Results for Variable Cross Sectionx150 and 4x2x150

	4x2x150	Variable Cross Section Areax150
Maximum Heat Flux on Gas Side Wall [MW/m ²]	29.83	29.82
Maximum Wall Temperature on Gas Side Wall [K]	770.5	772.2
Maximum Coolant Temperature [K]	647.3	675.2
Required Pressure Inlet for Coolant [bar]	110.8	78.4
Pressure Drop in Channel [bar]	50.8	18.4

As can be seen from Figure 6.27, velocity magnitude is high in throat region and low in combustion and nozzle exit regions. Therefore it is expected a better cooling efficiency in throat region relatively to combustion and nozzle exit regions. Since for both cases the cross section area is same in throat region, temperature values are quite similar in this region. But as we increased the cross section area the cooling efficiency is decreased and increases the local temperatures at larger cross section area regions (Figure 6.28 and Figure 6.29).

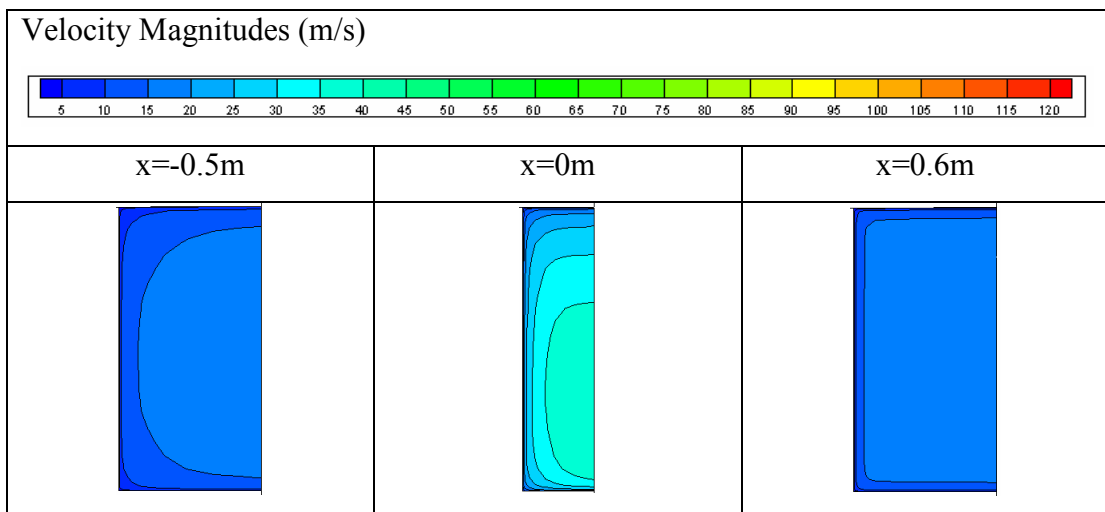


Figure 6.27 – Velocity Profiles of Coolant for Variable Cross Section Channel at Different Locations

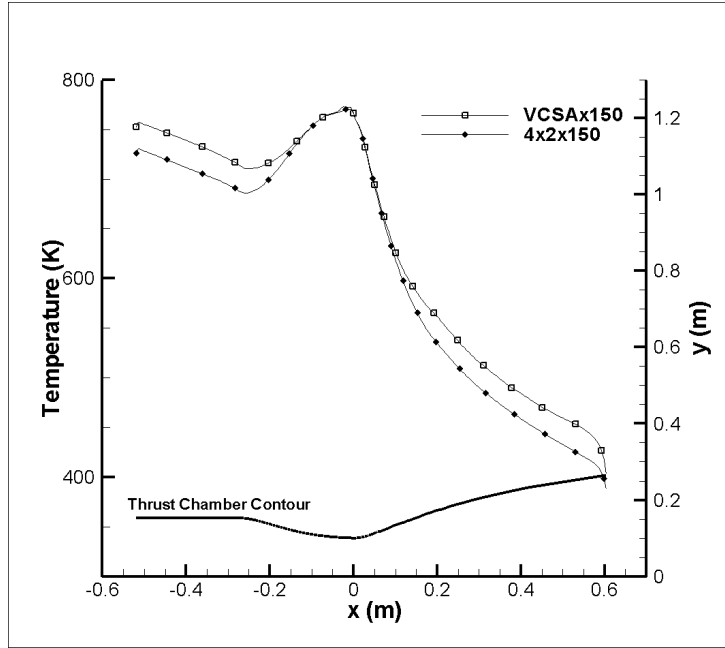


Figure 6.28 – Temperature Distribution on Gas Side Wall along Axial Direction for 8 mm Channel Height

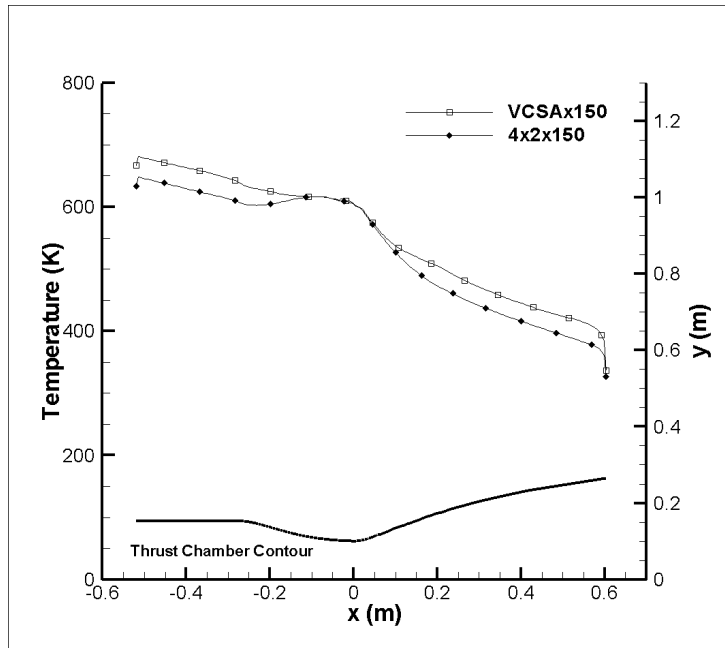


Figure 6.29 – Temperature Distribution of Coolant on Coolant Side Wall along Axial Direction for Variable Cross Section Area Investigation

As the velocity is decreased in larger cross section regions pressure drop is decreased also. In Figure 6.30 the pressure distribution along axial direction for 4x2x150 channel geometry and variable cross section area channel geometry is given. For variable cross section geometry the slope of pressure drop is low for larger cross section regions and the slope of pressure drop is high for smaller cross section region.

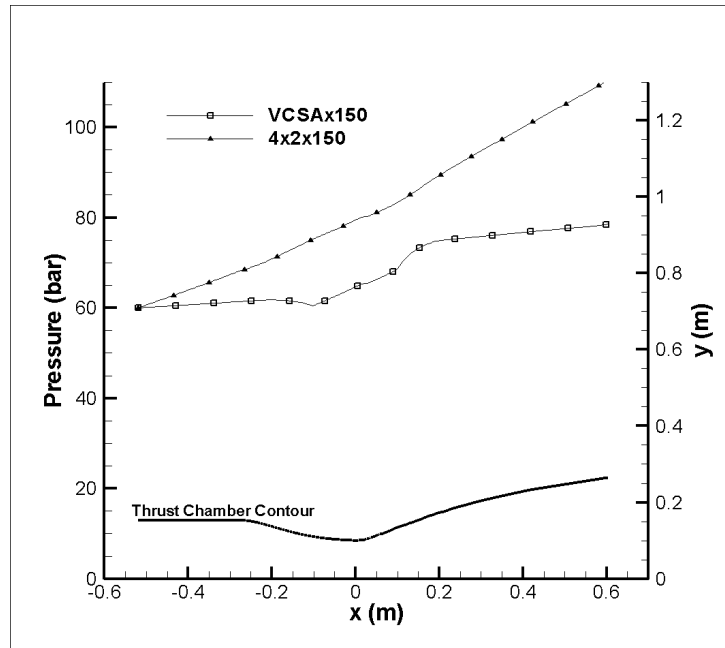


Figure 6.30 – Pressure Distribution of Coolant along Axial Direction for Variable Cross Section Area Investigation

16 different channel geometries are investigated and the variable cross section area channel geometry gives the best sufficient results from the engineering point of view although coolant temperature is reached higher temperature values compared with other geometries.

Maximum wall temperature on gas side wall is calculated as 770.5 K. For OFHC Copper melting temperature is 1083 °C (1356 K). Therefore we can conclude no

failure will be observed in thrust chamber because of the melting of the solid domain.

In Table 2.2 the critical temperature and critical pressure of Kerosen is given 678 K and 2.0 MPa (20 Bar). For the variable cross section channel geometry, the maximum temperature of the coolant is calculated as 675.2 K. This put the convection heat transfer on curve $B_1 - B_2$ in Figure 2.6. No boiling occurs in the coolant.

Pressure drop in the channel calculated as 18.4 bar which is quite sufficient for a regeneratively cooled rocket engine with 60 bar chamber pressure.

CHAPTER 7

CONCLUSION AND DISCUSSION

In this study, the effects of geometry and number of rectangular cooling channels on cooling efficiency are investigated in terms of the maximum temperature of thrust chamber wall and coolant, and the pressure drop in cooling channel of a liquid propellant rocket engine. The engine has been modeled to operate on a LOX/Kerosene mixture at a chamber pressure of 60 bar with 300 kN thrust.

10 different channel geometries are formed in 2 groups with 100 cooling channels and different constant cross-section area in axial direction. In each group the height of the cooling channels are constant and width of the channels are decreased gradually. For the first group channel height is 4 mm and for the second group channel height is 8 mm. Results are examined according to the maximum temperature of thrust chamber wall and coolant, and also pressure drop in cooling channel. From the engineering point of view the best cooling efficiency is obtained by $4 \times 2 \text{ mm}^2$ channel cross section area and 100 cooling channels with relatively high pressure drop.

Optimum number of cooling channels is found for the constant cross section area $4 \times 2 \text{ mm}^2$ and 150 cooling channels with a pressure drop 50.8 bar. By increasing the number of cooling channels 50%, the pressure drop in the cooling channel is decreased approximately 51%. To decrease the pressure drop in the cooling

channel more, cross-section area is increased in low heat flux regions up to 4x4 mm² and pressure drop is decreased to 18.4 bar (approximately 64%).

According to the analysis results following design rules for cooling channels can be summarized as:

- Increasing the aspect ratio with constant height and constant number of cooling channels, will increase the cooling efficiency up to a optimum level, then efficiency will decrease because of decreasing heat transfer area.
- Increasing the aspect ratio with constant height and constant number of cooling channels, will increase the pressure drop in cooling channel.
- Increasing the number of cooling channels without changing the geometry, will increase the cooling efficiency up to an optimum level with increasing total heat transfer area, then efficiency will decrease because of decreasing mass flow rate per channel.
- Increasing the number of cooling channels without changing the geometry, will decrease the pressure drop in channel.
- Increasing the cross section area of a channel in certain regions of the cooling channel, will decrease the cooling efficiency, increase the local temperatures and decrease the pressure drop in this region.

This thesis gives the analysis of regenerative cooling for a preliminary designed thrust chamber. As a future work, the parameters affecting the cooling efficiency can be optimized for given conditions. User defined function used for heat flux on gas side wall can be improved in consideration of turbulence effect in combustion region of thrust chamber.

REFERENCES

- [1] Huzel, D., K., Huang, D., H., “Modern Engineering for Design Liquid-Propellant Rocket Engines”, AIAA,1992.
- [2] Coulbert, C., D., “Selecting Cooling Techniques for Liquid Rockets for Spacecraft”, Journal of Spacecraft and Rockets, Vol. 1, 2, 1964.
- [3] Sutton G., P., “Rocket Propulsion Elements”, John Wiley & Sons, Inc., 6th Edition, 1992.
- [4] Batha, D., R., Carey, M., D., Campell, J., G., Coulbert, C., D., “Thrust Chamber Cooling Techniques for Spacecraft Engines”, Marquardt Corporation, NAS-7-103, 1963.
- [5] Sullivan, J., A., Y., “Numerical Analysis of Variable Property Flow Through Rectangular Channels”, The Pennsylvania State University, 1995.
- [6] Merkle C., L., Li, D., Sankaran, V., “Analysis of Regen Cooling in Rocket Combusters”, Jannaf Propulsion Conference, 2004.
- [7] Sanford, G., Bonnie, J., M., “Computer Program for Calculation of Complex Chemical Equilibrium Compositions and Applications” NASA RP-1311, 1994.
- [8] Zucrow, M., J., Hoffman, J., D., “Gas Dynamics: Multidimensional Flows”, vol. 1 & 2, John Wiley & Sons Inc., 1977.

- [9] Aksel, M., H., Eralp, O., C., “Gas Dynamics”, Prentice Hall., 1994.
- [10] Bucharsky V., L., “Sıvı Yakıtlı İtki Sistemleri Eğitim Notları”, METU, 2008.
- [11] Seçkin, B., “Rocket Nozzle Design and Optimization”, M. Sc. Thesis, METU, 2003.
- [12] Bartz, D., R., “A Simple Equation for Rapid Estimation of Rocket Nozzle Convective Heat Transfer Coefficients”, Technical Notes, California Institute of Technology, DA-04-495, 1957.
- [13] GAMBIT[®], <http://www.fluent.com/software/gambit/index.htm>
- [14] FLUENT[®], <http://www.fluent.com/software/fluent/index.htm>
- [15] Arpaci, V. S., Larsen, P. S., “Convection Heat Transfer”, Prentice Hall, Inc., 1984.
- [16] Wadel, M., F., “Comparison of High Aspect Ratio Cooling Channel Designs for a Rocket combustion Chamber with Development of an Optimized Design”, NASA/TM-1998-206313
- [17] Wadel, M., F., Meyer, M., L., “Validation of High Aspect Ratio Cooling in a 89 kN Thrust Chamber”, AIAA 96-2584, July 1996.
- [18] Sutton, G., P., “history of Liquid Propellant Engines in United States”, Journal of Propulsion and Power, Vol. 19, No. 6, 2003.
- [19] Naraghi, M., H., Dunn, S., Coats, D., “Dual Regenerative Cooling Circuits for Liquid Rocket Engines”, AIAA 2006-4367, July 2006.

- [20] Carlie, J., Quentmeyer, R., “An Experimental Investigation of High-Aspect-Ratio Cooling Passages”, AIAA 92-3154, July 1992.
- [21] Mitsubishi Materials, C003E General Catalogue, 2007-2009
- [22] Esposito, J., J., Zabora, R., F., “Thrust Chamber Life Prediction – Mechanical and Physical Properties of High Performance Rocket Nozzle Materials”, NASA CR – 134806, 1975.
- [23] Muraca, R., F., Whittick, J., S., “Materials Data Handbook – Inconel Alloy-718”, NASA CR – 123774, April 1972.
- [24] Naraghi, M., H., Dunn, S., Coats, D., “A Model for Design and Analysis of Regeneratively cooled for Rocket Engine”, AIAA 2004-3852, 2006.
- [25] Wang, T., Luong, V., “Hot-Gas-Side and Coolant-Side Heat Transfer in Liquid Rocket Engine Combustors”, Journal of Thermophysics and Heat Transfer, Vol. 8, No. 3, 1994.
- [26] Wang, Q., Wu, F., Zeng, M., Luo, L., “Numerical simulation and Optimization on Heat Transfer and Fluid Flow in Cooling Channel of Liquid Rocket Engine Thrust Chamber”, International Journal for Computer Aided Engineering and Software, Vol. 23, No. 8, pp. 907-921, 2006.
- [27] Schuff, R., Maier, M., Sindiy, O., Ulrich, C., Fugger, S., “Integrated Modeling and Analysis for a LOX/Methane Expander Cycle Engine: Focusing on Regenerative Cooling Jacket Design”, AIAA 2006-4534, July 2006.
- [28] Ciniaref, G., D., Dorovoliski , M., B., “Theory of Liquid-Propellant Rockets”, Moscow, 1957.

- [29] Barrere M., Jaumotte, A., Veubeke, B., F., Vandenkerckhove J., “Rocket Propulsion”, Elsevier Publishing Company, 1960.
- [30] Locke, J., M., “Analysis of Heat Transfer Correlations for Supercritical Hydrogen in Regenerative Cooling Channels”, The University of Alabama, 2005.
- [31] Taylor, M., F., “Prediction of Friction and Heat Transfer Coefficients with Large Variations in fluid Properties”, NASA TM-X-2145, 1970.
- [32] Sieder, E., N., Tate, G., E., “Heat Transfer and Pressure Drop of Liquids in Tubes”, Industrial and Engineering Chemistry, Vol. 28, No. 12, Dec. 1936, pp. 1492-1453.
- [33] McCarthy, J. R., Wolf, H., “Forced Convection Heat Transfer to Gaseous Hydrogen at High Heat Flux and High Pressure in a Smooth, Round, Electrically Heated Tube”, ARS Journal, 30, 1960, pp.423-424.
- [34] Aksel, M., H., “Notes on Fluid Mechanics”, METU, 1990.
- [35] Degarmo, E., P., Black, J., T., Kosher, R., A., “Materials and Processes in Manufacturing”, Macmillan Publishing Company, 7th Edition, 1988.

APPENDIX A

THERMAL PROPERTIES OF MATERIALS

Table A.1 – Thermal Properties of Kerosene

Density [kg/m ³]	820
Specific Heat [J/kg-K]	$C_p = -2.82 \times 10^{-8} \times T^2 - 2.95 \times 10^{-4} \times T + 0.261$
Thermal Conductivity [W/m-K]	$k = 9.64 \times 10^{-8} \times T^2 - 2.95 \times 10^{-4} \times T + 0.261$
Viscosity [kg/m-s]	$\mu = -1.46 \times 10^{-11} \times T^3 + 3.22 \times 10^{-8} \times T^2 - 2.39 \times 10^{-5} \times T + 6.00 \times 10^{-3}$

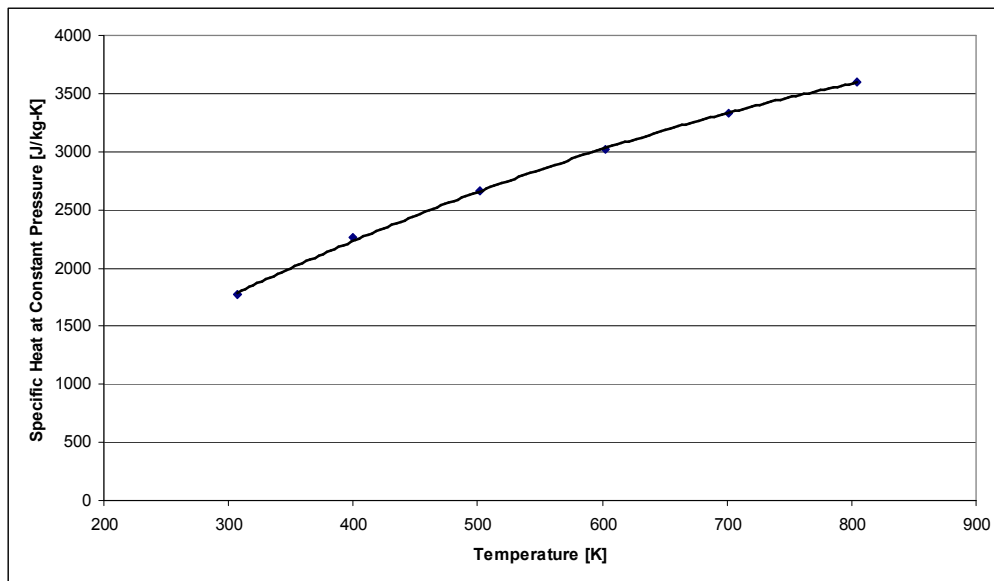


Figure A.1 – Temperature Variable C_p for Kerosene

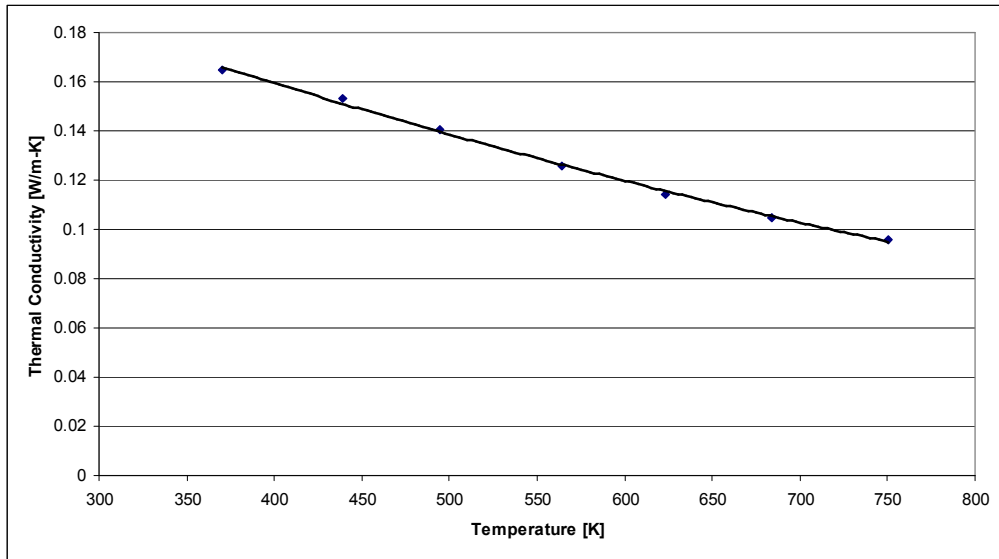


Figure A.2 – Temperature Variable Thermal Conductivity for Kerosene

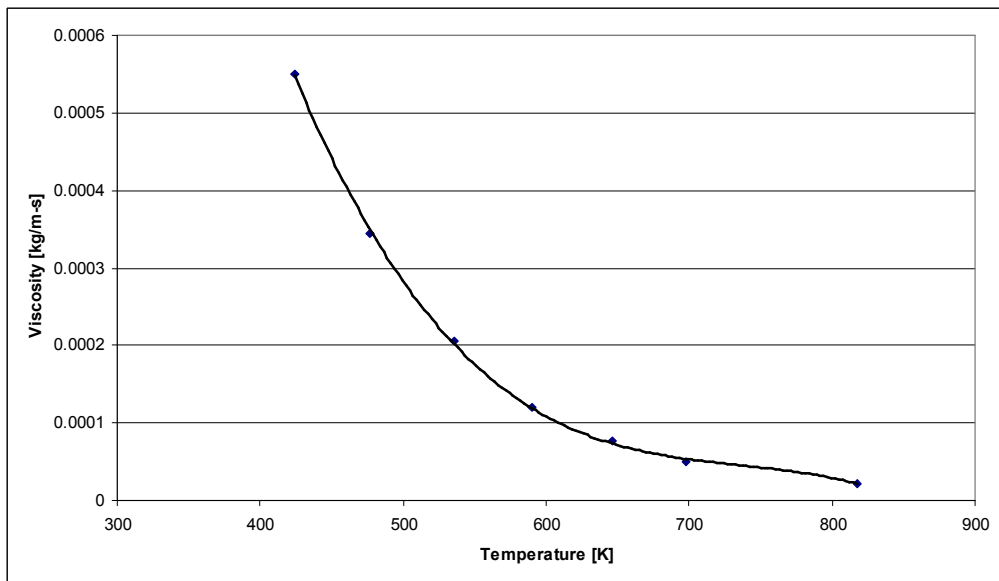


Figure A.3 – Temperature Variable Viscosity for Kerosene

Table A.2 – Thermal Properties of Liquid Hydrogen

Density [kg/m ³]	71
Specific Heat [J/kg-K]	$C_p = -5.85 \times 10^{-1} \times T^2 + 1.85 \times 10^2 \times T + 3.62 \times 10^3$ (between 30 – 195K) $C_p = -1.09 \times 10^{-4} \times T^3 + 1.53 \times 10^1 \times T^2 - 7.22 \times 10^1 \times T + 2.60 \times 10^4$ (between 195 – 550K)
Thermal Conductivity [W/m-K]	$k = 2.33 \times 10^{-7} \times T^2 + 2.05 \times 10^{-4} \times T + 0.141$
Viscosity [kg/m-s]	$\mu = -2.83 \times 10^{-6} T + 1.75 \times 10^{-4}$ (between 20 – 60K) $\mu = -4.45 \times 10^{-13} \times T^3 + 4.75 \times 10^{-10} \times T^2 - 1.40 \times 10^{-7} \times T + 2.06 \times 10^{-5}$ (between 60 – 550K)

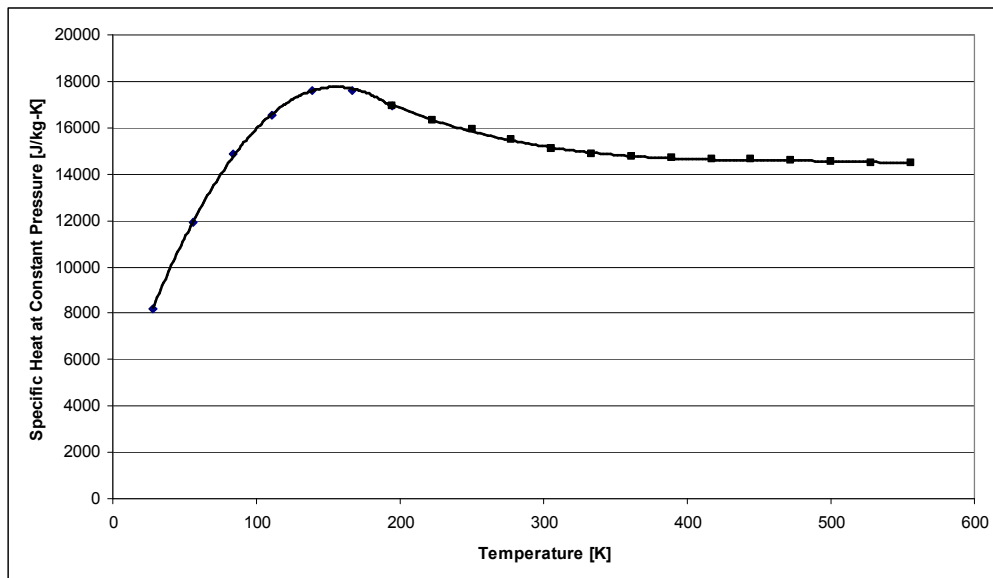


Figure A.4 – Temperature Variable C_p for Liquid Hydrogen

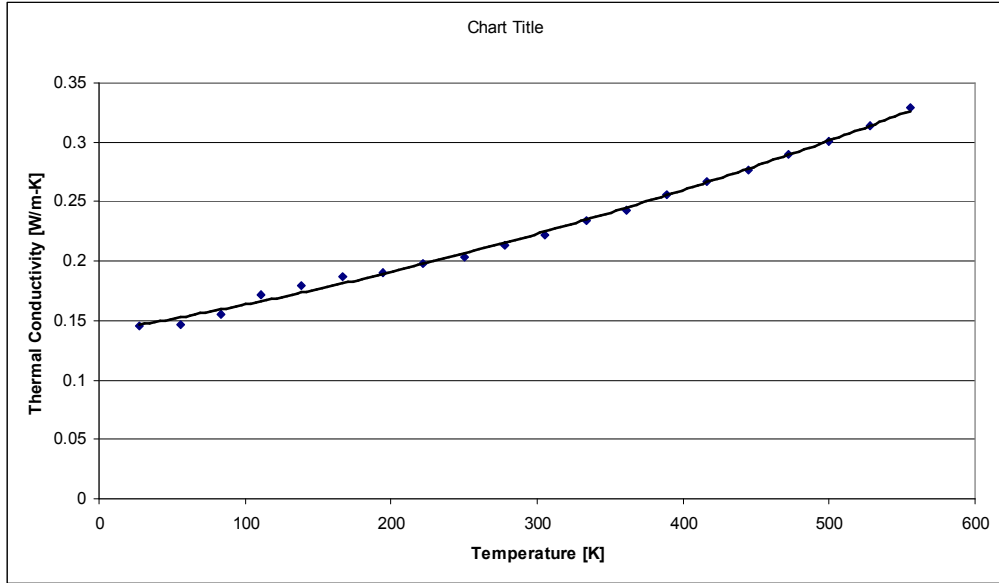


Figure A.5 – Temperature Variable Thermal Conductivity for Liquid Hydrogen

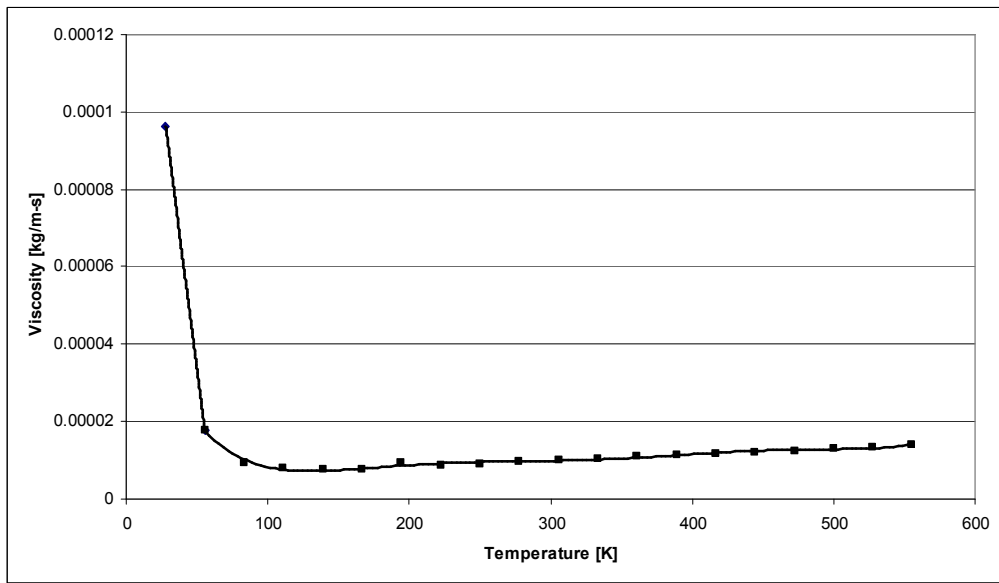


Figure A.6 – Temperature Variable Viscosity for Liquid Hydrogen

Table A.3 – Thermal Properties of OFHC Copper

Density [kg/m ³]	8890
Specific Heat [J/kg-K]	$C_p = 2.61 \times T - 39.2$ (between 20 – 123K) $C_p = 5.32 \times 10^{-6} \times T^3 - 6.17 \times 10^{-3} \times T^2 + 2.44 \times T + 64.7$ (between. 123 – 800K)
Thermal Conductivity [W/m-K]	$k = 1.10 \times 10^{-1} \times T^2 - 23.9 \times T + 1730$ (between 20 – 90K) $k = 6.66 \times 10^{-4} \times T^2 - 5.91 \times 10^{-1} \times T + 520$ (between 90 – 800K)

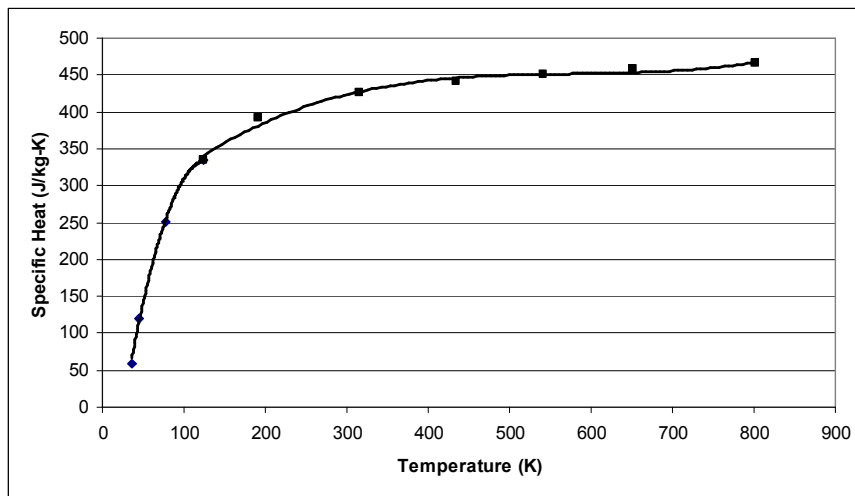


Figure A.7 – Temperature Variable C_p for OFHC Copper

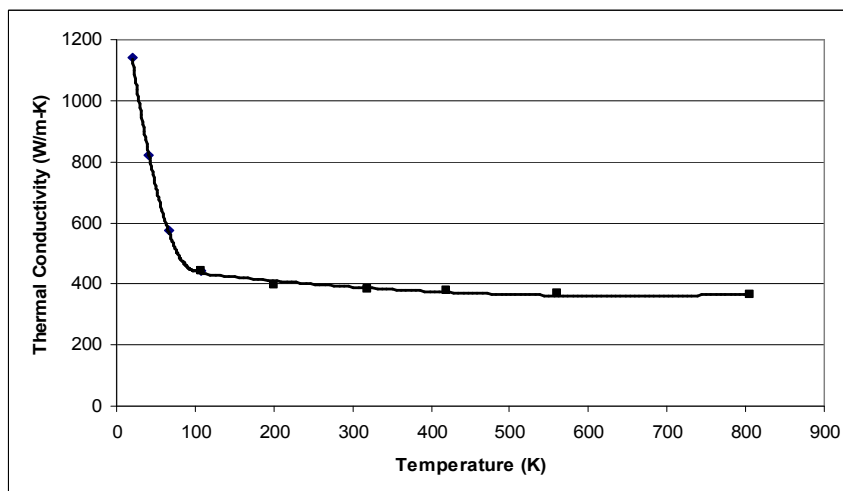


Figure A.8 – Temperature Variable Thermal Conductivity for OFHC Copper

Table A.4 – Thermal Properties of INCONEL 718

Density [kg/m ³]	8190
Specific Heat [J/kg-K]	$C_p = 5.79 \times 10^{-7} \times T^2 + 3.04 \times 10^{-1} \times T^{-1} + 327$
Thermal Conductivity [W/m-K]	$k = 1.44 \times 10^{-2} \times T + 7.4$

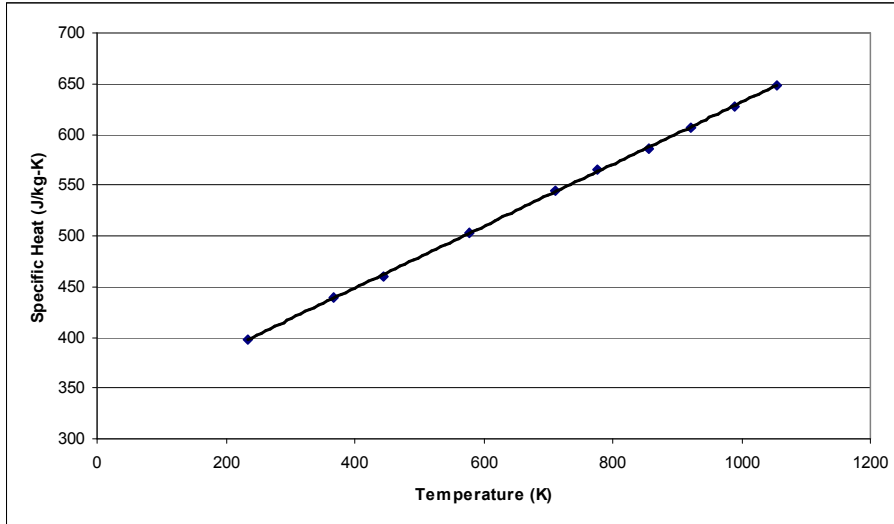


Figure A.9 – Temperature Variable C_p for INCONEL 718

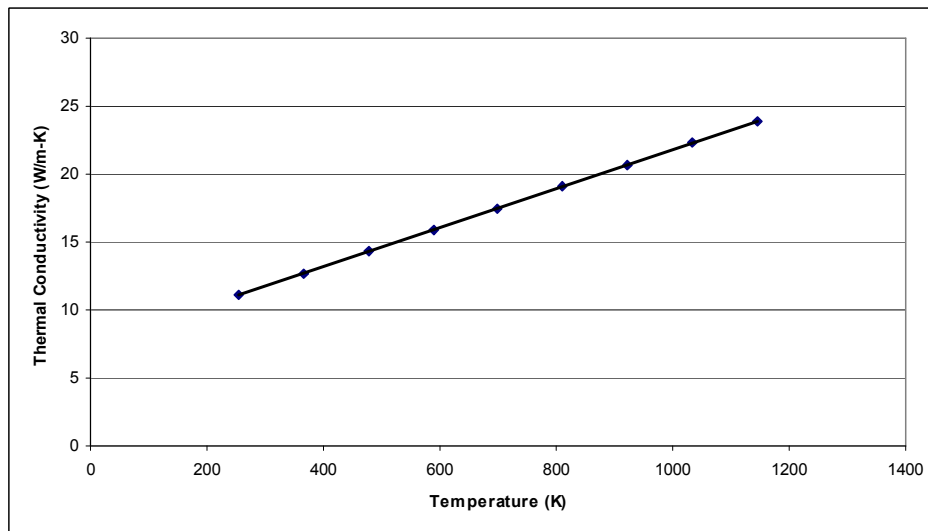


Figure A.10 – Temperature Variable Thermal Conductivity for INCONEL 718

APPENDIX B

USER DEFINED FUNCTION FOR HEAT FLUX ON GAS SIDE WALL

```

#include "udf.h"
# define pi (3.14159)

DEFINE_PROFILE(Boun_Cond, t, i)

{

real x[ND_ND];          /* this will hold the position vector */

real rt, dt, At, vis, Cp, Pr, Pc, Tc, gamma, Cstar, g, r, A, M, Mnew, N1, N2, N3, Taw, sigma, hgas,
func, ffunc, fCO2, fH2O, Le, qrad, qCO2, qH2O, P, Pcr;

face_t f;

int k,NI;

    rt=0.1;                /* m          */
    vis=0.00010863;        /* kg/m-s     */
    Cp=2083.3;             /* J/kg-K     */
    Pr=0.63;               /*            */
    Pc=6000000;            /* Pa         */
    Pcr=61.18297;          /* kg/cm2     */
    Tc=3570.44;            /* K          */
    gamma=1.146;           /*            */
    Cstar=1804.7;          /* m/s        */

    NI=100000;

    dt=rt*2;
    At=pi*pow(rt,2);

    fCO2=0.11917;          /* Mole Fraction of CO2 */
    fH2O=0.31769;          /* Mole Fraction of H2O */

begin_f_loop(f,t)

{

```

```

F_CENTROID(x,f,t);
r=sqrt(pow(x[a],2)+pow(x[1],2));
A=pi*pow(r,2);
Le=0.6*2*r;
/* For Combustion Region */
if (x[0]<0.28)
{
M=0;

P=Pcr/pow((1+(gamma-1)*pow(M,2)/2),(gamma/(gamma-1)));

Taw=Tc*((1+pow(Pr,0.33)*((gamma-1)/2)*pow(M,2))/
(1+((gamma-1)/2)*pow(M,2)));

sigma=pow((0.5*F_T(f,t)/Tc*(1+(gamma-1)*
pow(M,2)/2)+0.5),-0.68)*pow((1+(gamma-1)*pow(M,2)/2),-0.12);

hgas=0.026*pow(vis/dt,0.2)*Cp*pow(Pc/Cstar,0.8)*pow(At/A,0.9)*
sigma/pow(Pr,0.6);

/* Radiation Heat Transfer */

qCO2=4.0705*pow((P*fCO2*Le),1/3)*(pow((Taw/100),3.5)-
pow((F_T(f,t)/100),3.5));

qH2O=4.0705*pow(P*fH2O,0.8)*pow(Le,0.6)*
(pow((Taw/100),3)-pow((F_T(f,t)/100),3));

qrad=qCO2+qH2O;
}

/* For Subsonic Region */
if (x[0]<0 && x[0]>=0.28)
{
for(k=1;k<=NI;k++)
{
if(k==1)
M=0.05;
}
}

```

```

else
M=Mnew;

N1=2/(gamma+1);
N2=(gamma+1)/(2*(gamma-1));
N3=1+(gamma-1)*pow(M,2)/2;

func=pow(N1,N2)*pow(N3,N2)/M-A/At;
ffunc=-pow(N1,N2)*pow(N3,N2)*pow(M,-2)+
pow(N1,N2)*N2*pow(N3,N2-1)*(gamma-1);

Mnew=M-func/ffunc;

if(fabs(Mnew-M)<0.01)
break;

}

P=Pcr/pow((1+(gamma-1)*pow(M,2)/2),(gamma/(gamma-1)));

Taw=Tc*((1+pow(Pr,0.33)*((gamma-1)/2)*pow(M,2))/
(1+((gamma-1)/2)*pow(M,2)));

sigma=pow((0.5*F_T(f,t)/Tc*(1+(gamma-1)*
pow(M,2)/2)+0.5,-0.68)*pow((1+(gamma-1)*pow(M,2)/2),-0.12);

hgas=0.026*pow(vis/dt,0.2)*Cp*pow(Pc/Cstar,0.8)*pow(At/A,0.9)*
sigma/pow(Pr,0.6);

/* Radiation Heat Transfer */

qCO2=4.0705*pow((P*fCO2*Le),1/3)*(pow((Taw/100),3.5)-
pow((F_T(f,t)/100),3.5));

qH2O=4.0705*pow(P*fH2O,0.8)*pow(Le,0.6)*
(pow((Taw/100),3)-pow((F_T(f,t)/100),3));

qrad=qCO2+qH2O;

}

/* For Supersonic Region */

if (x[0]>=0)
{
for(k=1;k<=NI;k++)
{
if(k==1)
M=20;

```

```

else
M=Mnew;

N1=2/(gamma+1);
N2=(gamma+1)/(2*(gamma-1));
N3=1+(gamma-1)*pow(M,2)/2;

func=pow(N1,N2)*pow(N3,N2)/M-A/At;
ffunc=-pow(N1,N2)*pow(N3,N2)*pow(M,-2)+
pow(N1,N2)*N2*pow(N3,N2-1)*(gamma-1);

Mnew=M-func/ffunc;

if(fabs(Mnew-M)<0.01)
break;
}

P=Pcr/pow((1+(gamma-1)*pow(M,2)/2),(gamma/(gamma-1)));

Taw=Tc*((1+pow(Pr,0.33)*((gamma-1)/2)*pow(M,2))/
(1+((gamma-1)/2)*pow(M,2)));

sigma=pow((0.5*F_T(f,t)/Tc*(1+(gamma-1)*
pow(M,2)/2)+0.5,-0.68)*pow((1+(gamma-1)*pow(M,2)/2),-0.12);

hgas=0.026*pow(vis/dt,0.2)*Cp*pow(Pc/Cstar,0.8)*pow(At/A,0.9)*
sigma/pow(Pr,0.6);

/* Radiation Heat Transfer */

qCO2=4.0705*pow((P*fCO2*Le),1/3)*(pow((Taw/100),3.5)-
pow((F_T(f,t)/100),3.5));

qH2O=4.0705*pow(P*fH2O,0.8)*pow(Le,0.6)*
(pow((Taw/100),3)-pow((F_T(f,t)/100),3));

qrad=qCO2+qH2O;
}

F_PROFILE(f,t,i) = (hgas*(Taw - F_T(f,t))+qrad);
}

end_f_loop(f,t)
}

```